Electron-impact excitation of forbidden and allowed transitions in Fe II

S. S. Tayal*
Department of Physics, Clark Atlanta University, Atlanta, Georgia 30314, USA

O. Zatsarinny†
Department of Physics and Astronomy, Drake University, Des Moines, Iowa 50311, USA

(Received 11 May 2018; published 11 July 2018)

Extensive calculations are reported for electron collision strengths, rate coefficients, and transitions probabilities for a wide range of transitions in Fe II. The collision strengths were calculated in the close-coupling approximation using the *B*-spline Breit-Pauli *R*-matrix method. The multiconfiguration Hartree-Fock method in connection with adjustable configuration expansions and a semiempirical fine-tuning procedure is employed for an accurate representation of the target wave functions. The energy correction was also used in the scattering calculations by adding to Hamiltonian matrices prior to transformation to intermediate coupling. The spin-orbit interaction term was added to the final Hamiltonian matrices in scattering calculations. The close-coupling expansion contains 340 fine-structure levels of Fe II and includes all levels of the $3d^6 4s$, $3d^5 4s^2$, $3d^7$, and $3d^6 4p$ configurations, plus a few lowest levels of the $3d^5 4s 4p$ configuration. The effective collision strengths are obtained by averaging the electron collision strengths over a Maxwellian distribution of velocities at electron temperatures in the range from 10^2 to 10^5 K and are reported for all possible inelastic transitions between the 340 fine-structure levels. The present results are more extensive than the previous calculations and considerably expand the existing data sets for Fe II, allowing a more detailed treatment of the available measured spectra from different space observatories. Comparison with other calculations for collision rates and available experimental radiative rates is used to place uncertainty bounds on our collision strengths and to assess the likely uncertainties in the existing data sets.

DOI: 10.1103/PhysRevA.98.012706

I. INTRODUCTION

Accurate radiative and collision atomic data for iron-peak elements are of great importance in the analysis and diagnostics of a broad range of stellar and nebular spectra [1–5]. The singly ionized iron-peak elements are the dominant ionization stage and there is a need of accurate data for many lines to cover the broad metallicity ranges. The experimental atomic data are scarce and usually limited to a small number of transitions. The computational laboratory astrophysics represents a major source of such extensive high-quality atomic data.

The Fe II ion is the most abundant of iron-peak elements with a large number of lines in a broad wavelength region from the infrared to ultraviolet and has received extra special attention for the theoretical and experimental studies of the transition and collision rates. The Fe II forbidden lines in the near-IR and mid-IR band are prominent in the interstellar shocked gas and nebulae [3,4]. The 16 lowest Fe II levels can be easily excited because of small excitation energies. The transitions between these levels give rise to lines in the IR wavelength region in the 1 to 2.5 μm ground-based observations. The ratios of these lines provide excellent density diagnostics to the $n_e = 10^3$–10^5 cm^{-3} emitting region. The uncertainty in atomic data for the Fe II ion is the challenging limitation in the interpretation of line intensities. Despite the increased activities to produce atomic data of progressively larger size and better accuracy, the current Fe II spectral models still remain of limited accuracy and predictions and observations disagree by up to several factors in some cases.

The earlier theoretical works of increasing size and sophistication include Baluja *et al.* [6], Berrington *et al.* [7], Pradhan and Berrington [8], and Zhang and Pradhan [9]. Pradhan and Berrington included 38 selected quartet and sextet terms of the $3d^6 4s$, $3d^7$, and $3d^6 4p$ configurations in the nonrelativistic calculation to obtain collision strengths between these 38 LS terms. They noted strong coupling between the terms of the $3d^6 4s$ and $3d^6 4p$ configurations. Later, based on the assumption that the relativistic effects in Fe II are not very important compared to electron-electron correlation effects, Zhang and Pradhan [9] used a pair coupling transformation to determine collision strengths for the selected fine-structure transitions from the 38 LS-state results of Pradhan and Berrington [8]. These data for a long time have been used for diagnostics of astrophysical plasmas and they still can be found as recommended atomic data for Fe II in the CHIANTI database [10].

Two additional separate *R*-matrix calculations have been performed later by Bautista and Pradhan [11,12] in order to complement the Zhang and Pradhan [9] work by including the low-lying doublet and sextet even-parity states that were excluded from previous computations. Their first calculation includes the lowest 18 LS levels of Fe II, and the second calculation includes five additional terms, resulting in a 23-state LS-coupled approximation. Comparing the rate coefficients,

*stayal@cau.edu
†oleg.zatsarinny@drake.edu

they estimated uncertainties to be about 30% for most of the transitions considered. However, due to the omission of the higher lying $3d^6 4p$ levels these calculations cannot be considered as consistent. The quite different rate coefficients obtained from these three 38-state, 18-state, and 23-state models indicate that convergence has not yet been achieved.

A new set of sophisticated calculations for the electron scattering on Fe II has been proposed by Burke *et al.* [13] to be carried out at Queen's University of Belfast based on their newly developed parallel *R*-matrix program PRMAT. They expressed the confidence that the rapidly increasing power and availability of parallel computers should enable converged effective collision strengths to be calculated for electron collision with open *d*-shell iron peak elements over the next several years. As part of this program, Ramsbottom *et al.* [14–16] performed extensive *LS*-coupling *R*-matrix calculations using the PRMAT codes to study the convergence of configuration-interaction (CI) and close-coupling (CC) expansions in Fe II.

Their first model [14] included all 38 quartet and sextet *LS*-coupled states which can be formed from the three target configurations $3d^6 4s$, $3d^7$, and $3d^6 4p$ and they analyzed effective collision strengths for 112 quartet-to-sextet transitions. A limited comparison is made with earlier theoretical work and large differences have been found to occur at the temperatures considered. In particular, it is found that the inclusion or omission of some $(N+1)$-bound configurations in the Hamiltonian matrices describing the collision process can have a huge effect on the resulting effective collision strengths, by up to a factor of four in some cases. This model was extended by Ramsbottom *et al.* [15] to include the additional levels which arise from the $3d^5 4s^2$ and $3d^5 4s 4p$ configurations, giving 113 *LS*-coupled quartet and sextet target states. They concluded that in order to obtain close to converged low-energy partial wave collision strengths 21 further configuration functions should be included in the CI expansion of the target, incorporating two-electron excitations from the $3s$ and $3p$ shells to the $3d$ shell. This model was used by Ramsbottom *et al.* [16] to generate total effective collision strengths for 1785 transitions in Fe II between the considered quartet and sextet *LS* states, but they ignored all doublet states.

Later, Ramsbottom *et al.* [17,18] performed a Breit-Pauli *R*-matrix (BPRM) calculation by including 262 fine-structure levels of the 100 *LS* terms belonging to the $3d^6 4s$, $3d^7$, and $3d^6 4p$ configurations in the CC expansion. The results from the first calculation [17] are restricted to the transitions among the 16 lowest levels of Fe II corresponding to the $3d^6 4s\ ^6D, 3d^7\ ^4F, 3d^6 4s\ ^4D$, and $3d^7\ ^4P$ multiplets, whereas the second calculation [18] included only the optically allowed lines for transitions from the $3d^6 4s$ and $3d^7$ even-parity states to the $3d^6 4p$ odd-parity levels. Their target expansions included a limited number of configurations, namely, the main spectroscopic configurations plus additional correlation effects incorporated via the single $3d^6 4d$ configuration. The large influence of the CI effects learned in the previous *LS* calculations [14–16] was ignored here, probably due to the great computational efforts required to incorporate the effects in the Breit-Pauli approach. These BPRM calculations show significant differences from earlier calculations; however, they cannot be considered as complete or converged due to the limitations indicated above.

Bautista *et al.* [19] calculated radiative transition and collision rates for the forbidden transitions between the 52 lowest even-parity levels of the $3d^6 4s$, $3d^7$, and $3d^5 4s^2$ configurations and used their data in spectral modeling of Fe II emission in the infrared and optical regions and absorption in the UV region. In these calculations, they used several available computer codes to estimate uncertainties from the dispersion in atomic data obtained in different models. The thermally averaged collision strengths for forbidden transitions in Fe II have been estimated to have uncertainties of about 50% or less for stronger transitions, but much greater for the weaker transitions reaching factors of two or more in some cases.

A general conclusion from the above short review is that not a single available calculation has yet achieved convergence so as to provide accurate atomic parameters. The problem is mainly computational; the very large number of energy levels and transitions involved in the spectrum requires big CC expansions, whereas the accurate representation of the open $3d$-shell target states requires extensive CI expansions. Each calculation for such a complex atomic system as Fe II is a compromise in the choice of scattering model and the target representation depending on the available supercomputer allocations and the codes used. Most target representations of Fe II in previous calculations yield very inaccurate energies for the excited terms of the system, mainly due to computational restrictions on the target expansions. That in turn hampers the accuracy of resonance structures which may provide dominant contribution to the spin-forbidden or weak transitions. All previous calculations were performed by employing essentially the same method, namely, the widely used *R*-matrix close-coupling code of the Belfast group. As pointed out by Ramsbottom *et al.* [15], a tremendous challenge for electron collision calculations of open-shell systems such as Fe II is the accurate target description which is difficult to achieve with standard CI procedures. The individual orbitals in the $3d^6 4s$, $3d^7$, $3d^5 4s^2$, $3d^6 4p$, and $3d^5 4s 4p$ target configurations are very term dependent. Hence, computer codes that require a set of orthogonal one-electron orbitals, such as RMATRXI and RMATRXII or their parallel extensions, can only account for such term dependence by large CI expansions, involving a number of specially designed pseudo-orbitals. In this case, even experienced users need to consider a careful balance of the *N*-electron target structure and the $(N+1)$-electron collision problem.

Our *B*-spline *R*-matrix (BSR) method with nonorthogonal orbitals [20] is an alternative approach, which has several advantages for complex target systems such as Fe II. The use of term-dependent, and therefore nonorthogonal, sets of one-electron orbitals generally allows for a highly accurate target description with relatively smaller configuration expansions. This was first illustrated in the nonrelativistic benchmark calculations for electron collisions with Fe II [21] where the flexibility of the code allowed us to generate a target description of unprecedented accuracy for collision calculations. The purpose of the present work is to perform more elaborate and extensive calculations for the electron scattering from Fe II by using highly accurate target wave functions and by including fine-structure effects in the close-coupling expansions through the Breit-Pauli Hamiltonian. The direct use of the Breit-Pauli approach, however, is computationally not feasible for such

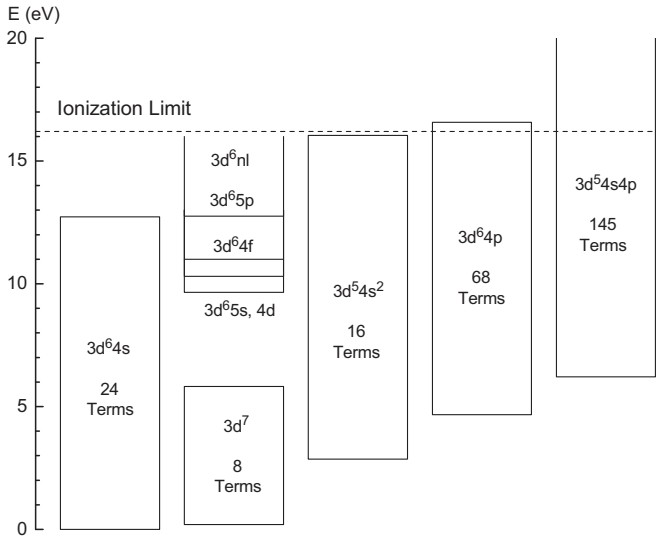

FIG. 1. Schematic diagram of the lower part of the Fe II spectrum.

complicated system as Fe II due to very extensive configuration expansions. The calculations, therefore, were carried out in two stages. First we consider the nonrelativistic *LS* transitions between all states of the $3d^64s$, $3d^7$, $3d^54s^2$, $3d^64p$, and $3d^54s4p$ target configurations giving rise to 261 overall *LS* terms. These data were then used to generate the Breit-Pauli Hamiltonian matrix for the transitions between fine-structure levels using the standard recoupling procedure. At this stage, for more accurate description of the spin-orbit mixing of different terms, the target *LS* energies were adjusted to the experimental values using the fine-tuning procedure, designed to represent the observed fine-structure splitting as accurately as possible. This procedure is close to the fine-tuning method which was successfully used by Hibbert and co-workers [22,23] for accurate calculations of the different radiative rates in Fe II. The available computer allocations allowed us to include 340 fine-structure levels of Fe II in the final close-coupling expansion. This set includes all levels of the $3d^64s$, $3d^54s^2$, $3d^7$, and $3d^64p$ configurations, plus a few lowest levels of the $3d^54s4p$ configuration. The final set of effective collision strengths includes the 57 630 transitions between the 340 fine-structure levels.

II. COMPUTATIONAL METHODS

A. Target wave function calculations

Figure 1 shows the energy level diagram of the lower part of the Fe II spectrum considered in the present calculations. The large number of possible terms resulting from the approximately half-open $3d$ shell, in combination with the near degeneracy of the $3d^7$, $3d^64s$, $3d^54s^2$, and other configurations, results in very complex spectra that are strongly influenced by configuration interaction. The electron correlation among the outer $3d$, $4s$, and $4p$ electrons is also expected to be important. The inclusion of the correlation effects requires considering at least single and double promotions of the valence electrons to the excited orbitals. In the case of the open $3d$ shell, inclusion of all important promotions leads to extremely large configuration expansions and makes it difficult to obtain accurate wave functions within standard multiconfiguration Hartree-Fock (MCHF) or configuration-interaction methods.

Another complication arises from the term dependence of the valence orbitals, which slows down the convergence of the multiconfiguration expansions. An important aspect of the present approach, which distinguishes it substantially from nearly all other methods commonly used to describe electron-atom collisions, is the possibility of using nonorthogonal one-electron orbitals in the multiconfiguration description of the N-electron target states. As a result, accurate description of both the energy levels and oscillator strengths can be achieved with more compact CI expansions. In traditional methods with an orthogonal set of one-electron orbitals, a similar accuracy can, in principle, be achieved by very large expansions using additional correlated pseudo-orbitals. In the calculations of the Fe II target states, we tried to account for all main correlation effects, while bearing in mind that the final multiconfiguration expansion still needs to be dealt with in the subsequent scattering calculation with one more electron to couple.

In the present work, we used the MCHF code of Froese-Fischer *et al.* [24] in combination with our CI code with nonorthogonal orbitals to generate the target wave functions. First, the inner $1s$, $2s$, $2p$, $3s$, and $3p$ orbitals were obtained from a Hartree-Fock calculation of the ground state. Keeping these orbitals frozen, we then generated the $3d$, $4s$, and $4p$ valence orbitals specifically for each principal configuration in the term-average approximation. The term dependence of the valence orbitals was found to be noticeable but not extremely strong, with maximum change of mean radius up to 10%. However, the corresponding corrections in the configuration energies are around 0.2 Ry, which makes the inclusion of term dependence very important for accurate calculation of the term energies. The above spectroscopic orbitals were supplemented with the $4l$ and $5l$ ($l = 0$–3) correlated orbitals. The correlation orbitals were also determined for each principal configuration separately and were generated with the MCHF program [24] for one specific term. These orbitals are then used for all terms of a given configuration.

The final configuration expansions contain all the most important one- and two-electron excitations from the valence $3d$, $4s$, and $4p$ orbitals of the principal configurations. Inclusion of all possible promotions for the given case of the open $3d$ shell leads to very large configuration expansions, with thousands of individual atomic configuration states differing in the intermediate terms. As illustrated in the recent calculations of oscillator strengths [23], convergence of the multiconfiguration expansions in Fe II is very slow, resulting in the expansion with tens of thousands of configurations. Such target expansions cannot be used in the scattering calculations. In the previous scattering calculations discussed above it is not clear how the specific target expansions were designed. Most likely these calculations included only so many configurations as allowed by the available computational resources. In the present approach, we attempted to include the most important correlation effects for the Fe II target states, and at the same time kept the target expansions to a reasonable size. To do that, we first analyzed the extended target expansions which contains *all* double promotions to determine the main correlation configurations.

TABLE I. Main correlation contributions.

Main configuration	Correlation configuration	Contribution
$3d^6 4s$	$3d^4 4d_1^2 4s$	0.0394
	$3d^5 4p_2^2$	0.0288
	$3d^5 4d_1 4s$	0.0284
	$3d^4 4f_1^2 4s$	0.0254
	$3d^5 4p_2 4f_2$	0.0215
	$3d^6 5s_3$	0.0210
$3d^7$	$3d^5 4d_1^2$	0.0467
	$3d^5 4f_1^2$	0.0245
	$3d^5 4p_1^2$	0.0240
	$3d^6 4d_1$	0.0239
$3d^5 4s^2$	$3d^5 4p_3^2$	0.1808
	$3d^5 4s 5s_3$	0.0371
	$3d^4 4d_1 4s^2$	0.0336
	$3d^3 4d_1^2 4s^2$	0.0304
	$3d^4 4s 4p_2 4f_2$	0.0258
	$3d^3 4f_1^2 4s^2$	0.0236
	$3d^4 4s 4p_2^2$	0.0236
	$3d^5 5s_3^2$	0.0234
	$3d^5 4d_3^2$	0.0228
	$3d^5 4s 4d_3$	0.0211
$3d^6 4p$	$3d^5 4p 5s_2$	0.0502
	$3d^4 4d_1^2 4p$	0.0397
	$3d^6 5p_3$	0.0370
	$3d^5 4d_1 4p$	0.0345
	$3d^4 4f_1^2 4p$	0.0298
	$3d^5 4f_2 5s_2$	0.0286
	$3d^5 5s_2 5p_2$	0.0240
	$3d^5 4s_2 5s_2$	0.0226
	$3d^5 4d_2 4f_2$	0.0203
	$3d^5 4d_2 5p_2$	0.0196
$3d^5 4s 4p$	$3d^5 4s 5p_3$	0.0497
	$3d^5 4p_3 4d_3$	0.0494
	$3d^3 4d_1^2 4s 4p$	0.0426
	$3d^3 4f_1^2 4s 4p$	0.0223
	$3d^4 4p^2 4f_2$	0.0216
	$3d^5 5s_3 5p_3$	0.0182
	$3d^5 4s 4f_3$	0.0180

In Table I, we list the main correlation configurations together with their average mixing coefficients. The orbitals with an additional subindex are the correlated orbitals from different nonorthogonal sets. Note that the correlated orbitals differ considerably from the corresponding spectroscopic orbitals and have mean radii close to the valence $3d$, $4s$, and $4p$ orbitals in the principal configurations. As seen from the table, the correlation pattern for different principal configurations is different and cannot be considered on the same footing. It may be noted that the major correlation corrections come from the $3d^2$-$4d^2$ substitution, along with other double promotions $3d^2$-$4p^2$ and $3d^2$-$4f^2$. Such configurations were only partly included in previous calculations. For example, Ramsbottom *et al.* [16] and Bautista *et al.* [19] included $3d^5 4d^2$ configurations, but none of the $3d^4 4d^2 4s$ or $3d^3 4d^2 4s^2$ configurations. This may bring an imbalance in the relative position of terms. The above double substitution reflects the $3d$ inner-shell correlation, which is expected to be different for the $3d^6 4s$, $3d^7$, and $3d^5 4s^2$ principal configurations due to different numbers of $3d$ electrons. Ramsbottom *et al.* [16] also found a large contribution from the double promotion of the more deep $3p$ shell. This promotion reflects the $3p$ inner-shell correlation which is expected to be the same for all considered states and thereby would not effect the relative position of terms. For this reason, we did not include such configurations in the present expansions.

As seen from Table I, we additionally found that the $3d$-$4f$ promotion also contributes significantly to correlation effects. No such configurations were included in the previous calculations. Note that $4f$ correlated orbitals have a mean radius close to the $3d$ orbital, and this explains its large influence. For the $3d^6 4s$ states it is also important to include the $3d$-$4s$ intershell correlation, which is reflected in the large contributions of the $3d^5 4p^2$ and $3d^5 4p 4f$ configurations, which correspond to the dipole interactions $3d4s$-$4p^2$ and $3d4s$-$4p4f$, respectively. The same concerns the $3d$-$4p$ intershell correlation in the $3d^6 4p$ states. This is reflected in the large contribution of the $3d^5 4p 5s$ configuration that corresponds to the $3d4p$-$4p5s$ dipole interaction. The $3d^6 4s^2$ states show strong mixing with the $3d^6 4p^2$ configuration, and for the $3d^6 4s 4p$ states the valence correlation between two outer electrons is reflected in the large contribution of the $3d^5 4s 5p$ and $3d^5 4p 4d$ configurations.

The above analysis allows us to choose the most important configurations which should be included in the final target expansions and, at the same time, to keep these expansions of manageable size, appropriate for the scattering calculations. We chose to keep all configurations with mixing coefficients more than $\sim$0.025. This resulted in CI expansions of size from 200 to 400 for each LS target state, suitable for the scattering calculations with the modern computational facilities. At this stage we also applied the first semiempirical correction using the above cutoff parameter to adjust the theoretical LS energies to experiment obtained by taking a weighted average over the fine-structure levels [25]. Due to different convergence of different terms, this required varying cutoff parameters in the range from 0.015 to 0.030 for the different terms. With this procedure, we managed to reach agreement with the observed LS energies of less than 0.1 eV for all included states.

As the next step, we obtained the J-dependent target states by diagonalizing the Breit-Pauli Hamiltonian on the basis of multiconfiguration LS wave functions described above, using the configuration-interaction procedure and nonorthogonal orbitals [26,27]. The target expansion, for total angular momentum J and parity π, have the form

$$\Psi^{\beta J\pi} = \sum_{\alpha LS} C(\beta J\pi; \alpha LS\pi)\Phi^{\alpha LS\pi}. \quad (1)$$

We included all one-electron Breit-Pauli operators, and no cutoff factor has been applied at this stage. The final target expansions contain on average 1000 configurations and still can be used in the collision calculations with available computational resources. Note that functions $\Phi^{\alpha LS\pi}$ in the above equation are the multiconfigurational expansions from the LS calculations, where coefficients for individual configurations were frozen. The diagonalization of the Breit-Pauli atomic Hamiltonian provides then only the coefficients $C(\beta J\pi; \alpha LS\pi)$, which describe the spin-orbit mixing of different LS terms. Accurate representation of the term mixing is very important for accurate description of transitions between the fine-structure levels.

This mixing crucially depends on both the spin-orbit interaction and the energy separation between the LS states. In order to improve the term mixing, we made additional semiempirical corrections to the energies of the $\Phi^{\alpha LS\pi}$ functions in such a way that the final fine-structure LSJ levels agree with the observed levels as closely as possible. These corrections are relatively small (less than 0.1 eV) but considerably improve the agreement with observed spectrum of the Fe II discussed below. Such fine-tuning of the LS terms is frequently used in the structure calculations [22,23] and aims to improve the description of the forbidden fine-structure transitions which crucially depends on the mixing coefficients.

B. Collision calculations

For the scattering calculations we employed the parallelized version of the BSR code [20] which is based on the R-matrix method. The BSR code was substantially modified and extended for the present calculations. The distinctive feature of the code is the use of B splines as a universal basis to represent the scattering orbitals in the inner region, $r \leqslant a$. Hence, the R-matrix expansion in this region takes the form

$$\begin{aligned}\Psi_k(x_1,\ldots,x_{N+1}) &= \mathcal{A}\sum_{ij}\bar{\Phi}_i(x_1,\ldots,x_N;\hat{\mathbf{r}}_{N+1}\sigma_{N+1})\,r_{N+1}^{-1}\,B_j(r_{N+1})\,a_{ijk} \\ &+ \sum_i \chi_i(x_1,\ldots,x_{N+1})\,b_{ik}. \end{aligned} \quad (2)$$

Here $\mathcal{A}$ denotes the antisymmetrization operator, $\bar{\Phi}_i$ are the channel functions, while the splines $B_j(r)$ represent the continuum orbitals. The principal advantage of B splines is that they form an effectively complete basis, and hence no Buttle correction to the R matrix is needed in this case. The amplitudes of the wave functions at the boundary, which are required for the evaluation of the R matrix, are given by the coefficient of the last spline, which is the only spline with nonzero value at the boundary.

The other important feature of the present code concerns the orthogonality requirements for the one-electron radial functions. The χ_i function in the above equation is additional $(N+1)$-electron bound states. In the standard R-matrix calculations [28], the latter are included one configuration at a time to ensure completeness of the total trial wave function and to compensate for orthogonality constraints imposed on the continuum orbitals. The use of nonorthogonal orbitals allows us to reduce or even to avoid the introduction of additional $(N+1)$-electron terms in the R-matrix expansion. We impose only limited orthogonal conditions to the continuum orbitals. In the present calculations we only require the orthogonality of continuum orbitals to the bound orbitals in the filled $1s$, $2s$, $2p$, $3s$, and $3p$ shells. No orthogonality constraints to the spectroscopic excited orbitals or the correlated orbitals were imposed. Thus the $(N+1)$-electron configurations χ_i can be completely avoided. This allows us to use much more extensive multiconfiguration expansions for target states and avoid the pseudoresonance structure which usually appears in the standard R-matrix calculations due to inconsistency of the scattering and bound parts of the close-coupling expansions.

The BSR code previously was applied for several iron ions [29–31] in the direct Breit-Pauli mode. That means the calculations of collision strengths in the intermediate coupling by including fine-structure effects directly in the solutions of scattering equations. In the present case of Fe II, such direct Breit-Pauli calculations are not possible due to extensive target expansions and the large number of scattering channels. Therefore, we chose to perform calculations in two stages, first the LS calculations for transitions between LS terms, and then a transformation of the Hamiltonian matrix in the inner region to the intermediate coupling. This scheme provides the same level of accuracy, but avoids repeating calculations of matrix elements for the nonrelativistic Hamiltonian for the different J values.

In the first step, we obtained the nonrelativistic Hamiltonian matrices in the inner region for the close-coupling equation containing *all* LS terms of the $3d^64s$, $3d^54s^2$, $3d^7$, $3d^64p$, and $3d^54s4p$ configurations. Overall it includes 261 LS levels, and the CC expansions for the e-Fe II scattering problem contains up to 818 different scattering channels in the LS-coupling scheme. We consider all partial waves up to $L = 50$ and total spin $S = 0$–3, with the overall number of partial waves equaling 510. The continuum orbitals in the internal region with radius $a = 25\ a_0$ were represented by 78 B splines of order 8. This leads to the Hamiltonian matrices with dimensions up to 60 000. The characteristic feature of the present Fe II calculation is the large configuration expansions for the total scattering functions and the extremely large number of different two-electron matrix elements. Partly this is due to open $3d$-shell configurations, but the main complication comes from the huge number of overlap factors due to the nonorthogonal orbitals. This required further optimization of the code for the determination of the angular coefficients and subsequent construction of the Hamiltonian matrix. In particular, the previous standard procedure to calculate first the angular coefficient using the BSR_BREIT program and then set up the Hamiltonian matrix using the BSR_MAT program cannot be applied in the present case due to the large size of the intermediate files of the angular coefficients that may reach several hundreds of Gb. We combined these two programs into one, BSR_BMAT, to calculate the angular coefficients for given configurations and then dynamically added the corresponding integrals to the Hamiltonian matrix. This procedure treats the Hamiltonian matrix in parts, and adds to the flexibility of performing calculations. The calculation of one partial wave required from 1 to 24 hours on the supercomputer with 1000 processors.

Having calculated the LS Hamiltonian matrix, the Breit-Pauli matrices have been then constructed using the transformation to the intermediate coupling scheme. It was performed in three steps. First, we modified the LS Hamiltonian matrices according to the fine-tuning of LS term energies discussed above. In the case of the orthogonal one-electron orbitals this is a trivial procedure which is reduced just to modification of the diagonal matrix elements. In the case of nonorthogonal orbitals, the Schrödinger equation reduces to the generalized eigenvalue problem

$$HC = SCE, \quad (3)$$

where S is the overlap matrix. Let us denote the energy corrections by the diagonal matrix D. As discussed in the BSR description [20], the above matrix equation is then transformed to

$$(H + S^{1/2} D S^{1/2}) C = S C E, \tag{4}$$

where the final correction is defined by the $S^{1/2} D S^{1/2}$ term. This correction was added to the Hamiltonian matrix in the internal region for all partial waves.

In the next step, we transform the Hamiltonian matrices in the internal region to the jK coupling using the equation

$$H(\alpha_i L_i S_i J_i l_i K_i J; \alpha_f L_f S_f J_f l_f K_f J) = \sum_{LS} T_{LS,J_i K_i}\ H(\alpha_i L_i l_i L S_i S; \alpha_f L_f l_f L S_f S)\ T_{LS,J_f K_f}, \tag{5}$$

where the transformation coefficient is given by

$$\begin{aligned} T_{LS,J_i K_i} &= \langle [(L_i l_i) L, (S_i s) S], J | [(L_i S_i) J_i, l_i] K_i, s, J \rangle \\ &= (-1)^{(s - l_i + J - J_i)} \sqrt{(2L+1)(2S+1)(2J_i+1)(2K_i+1)} \\ &\quad \times \begin{Bmatrix} L & S & J \\ s & K_i & S_i \end{Bmatrix} \begin{Bmatrix} L_i & l_i & L \\ K_i & S_i & J_i \end{Bmatrix}. \end{aligned} \tag{6}$$

Now we can use term-coupling coefficients from Eq. (1) to transform Hamiltonian matrices in the jK coupling to full intermediate coupling:

$$\begin{aligned} H(\beta_i J_i l_i K_i J; \beta_f J_f l_f K_f J) &= \sum_{\alpha_i L_i S_i \alpha_f L_f S_f} C(\beta_i J_i; \alpha_i L_i S_i) \\ &\quad \times H(\alpha_i L_i S_i J_i l_i K_i J; \alpha_f L_f S_f J_f l_f K_f J)\ C(\beta_i J_i; \alpha_i L_i S_i). \end{aligned} \tag{7}$$

This part of the calculations was performed with the program BSR_RECOUP which is a new program in the BSR complex.

In the last, third step, the final Hamiltonian matrices were augmented by adding the spin-orbit interaction term related to the scattering electron. Thus the above scheme is completely equivalent to the direct Breit-Pauli calculations. The advantage is its flexibility. Computationally, this scheme allows us to divide the full calculations in the moderate three steps and consider much more extensive models as used in the Breit-Pauli calculations for simpler atomic systems. It also allows us to avoid repeating calculations of the same LS matrix elements for the different J. The above scheme also allows us to apply the energy fine-tuning of the LS terms, that in turn improves the description of the target spin-orbit mixing which is important for spin-forbidden transitions between fine-structure levels of Fe II. It was an important reason in choosing this computational scheme.

Our final intermediate-coupling model contains 340 fine-structure levels of Fe II and includes all levels of the $3d^6 4s$, $3d^5 4s^2$, $3d^7$, and $3d^6 4p$ configurations, plus a few lowest levels of the $3d^5 4s 4p$ configuration. This model will be afterwards denoted as BSR-340. At present, we are not able to include all 716 fine-structure levels for the above configurations, mainly due to the computational reasons. Direct numerical calculations were performed for 82 partial waves, with total electronic angular momentum up to $J = 40$, for both even and odd parities. This requires inclusion of all LS partial waves up to $L = 50$. The maximum number of channels in a single partial wave was 2354. With a basis size of 78 B splines, this required the diagonalization of matrices with dimensions up to 160 000. The calculations were carried out with parallelized versions of the BSR complex, using supercomputers with distributed memory. Such extensive calculations were made possible by the NSF XSEDE grant.

The asymptotic solutions in the outer region and subsequently the collision parameters were calculated with the parallel version of the STGF program [32]. In the resonance region for impact energies below the excitation energy of the highest level included in the CC expansion, we used a fine energy step of 10^{-4} Ry to properly map resonance structures. For energies above the highest excitation threshold included in the CC expansion, the collision strengths vary smoothly, and hence we chose a coarser electron energy step of 10^{-2} Ry. We calculated collision strengths up to 10 Ry, which is enough to achieve the asymptotic region. Altogether, 12 000 energies for the colliding electron were considered. For even higher energies, we extrapolated collision strengths Ω using the well-known asymptotic energy dependence of the various types of transitions. The included partial waves are sufficient to achieve convergence for forbidden transitions at all energies. Additional partial wave contributions are needed for high electron energies in the case of the dipole-allowed transitions. These contributions were estimated with a top-up procedure based on the Coulomb-Bethe method or on geometric series approximation.

To obtain effective collision strengths $\Upsilon(T_e)$, we convoluted the collision strength Ω with a Maxwellian distribution for electron temperature T_e, i.e.,

$$\Upsilon_{i-j}(T_e) = \int_{E_{th}}^{\infty} dE\ \Omega_{i-j}(E)\ \exp\left(\frac{E - E_{th}}{k T_e}\right). \tag{8}$$

Here E_{th} is the i-j transition energy and k is the Boltzmann constant. We calculated Υ for temperatures from 10^2 to 10^5 K.

III. RESULTS AND DISCUSSION

A. Target energies and radiative parameters

Table II compares the calculated target excitation energies with the experimental values. Experimental excitation energies are taken from the NIST compilation [25] where possible, but for some of the higher lying levels no observed values are available. Note that the NIST database presents the excitation energies with accuracy up to 9 significant digits. The full list of levels included in the present scattering calculations is given in the Supplemental Material [37]. As in the NIST compilation, the levels in the table are ordered according to their LS terms. The energy level position is defined by the index given in the first column. This index will be referred to in the following discussion to denote a particular transition. The present excitation energies agree closely with experimental energies; the difference for most levels is less than 0.01 eV. The order of the levels also agrees with the observed spectrum for most of the levels, with the first different ordering detected only for level 106. The agreement with the experimental

TABLE II. Excitation level energies and lifetimes for Fe II.

Level				Energy (eV)			Lifetime (s)			
Index	Configuration	Term	J	Present	NIST[a]	Diff.	Present	B2016[b]	HD2011[c]	Expt.
1	$3d^6(^5D)4s$	$a\ ^6D$	9/2	0.00000	0.00000	0.000				
2			7/2	0.04744	0.04771	0.000	4.67×10^2	4.72×10^2	4.67×10^2	
3			5/2	0.08244	0.08278	0.000	6.35×10^2	6.37×10^2	6.33×10^2	
4			3/2	0.10658	0.10695	0.000	1.39×10^3	1.39×10^3	1.39×10^3	
5			1/2	0.12077	0.12114	0.000	5.28×10^3	5.29×10^3	5.29×10^3	
6	$3d^7$	$a\ ^4F$	9/2	0.22723	0.23217	−0.005	3.87×10^4	1.47×10^4	7.06×10^3	
7			7/2	0.30092	0.30130	0.000	1.70×10^2	1.69×10^2	1.66×10^2	
8			5/2	0.35525	0.35186	0.003	2.53×10^2	2.51×10^2	2.48×10^2	
9			3/2	0.39264	0.38652	0.006	7.02×10^2	6.94×10^2	6.84×10^2	
10	$3d^6(^5D)4s$	$a\ ^4D$	7/2	0.98570	0.98633	−0.001	8.12×10^1	6.76×10^1	7.12×10^1	
11			5/2	1.04058	1.04047	0.000	8.88×10^1	7.25×10^1	7.70×10^1	
12			3/2	1.07705	1.07624	0.001	1.00×10^2	7.94×10^1	8.60×10^1	
13			1/2	1.09811	1.09686	0.001	1.08×10^2	7.94×10^1	9.24×10^1	
14	$3d^7$	$a\ ^4P$	5/2	1.66597	1.67062	−0.005	3.03×10^1	2.00×10^1	1.91×10^1	
15			3/2	1.69561	1.69526	0.000	3.46×10^1	2.20×10^1	2.10×10^1	
16			1/2	1.72941	1.72398	0.005	3.48×10^1	2.20×10^1	2.10×10^1	
17	$3d^7$	$a\ ^2G$	9/2	1.96117	1.96449	−0.003	4.47	4.81	3.98	
18			7/2	2.03119	2.02955	0.002	8.15	8.85	7.25	
19	$3d^7$	$a\ ^2P$	3/2	2.27492	2.27643	−0.002	5.71	5.15	4.54	
20			1/2	2.34326	2.34166	0.002	9.85	9.01	7.89	
21	$3d^7$	$a\ ^2H$	11/2	2.52034	2.52187	−0.002	5.67×10^1	6.67×10^1	5.12×10^1	
23			9/2	2.58197	2.57959	0.002	1.40×10^1	1.65×10^1	1.28×10^1	
22	$3d^7$	$a\ ^2D$	5/2	2.53930	2.54378	−0.004	2.33	2.30	1.89	
26			3/2	2.64821	2.64186	0.006	1.74	1.77	1.50	
24	$3d^6(^3P)4s$	$b\ ^4P$	5/2	2.58690	2.58266	0.004	9.67×10^{-1}	8.62×10^{-1}	8.56×10^{-1}	
30			3/2	2.70529	2.70435	0.001	7.78×10^{-1}	6.99×10^{-1}	6.88×10^{-1}	
31			1/2	2.78459	2.77846	0.006	7.08×10^{-1}	6.62×10^{-1}	6.26×10^{-1}	
25	$3d^6(^3H)4s$	$a\ ^4H$	13/2	2.63882	2.63486	0.004	2.19	1.83	2.10	
27			11/2	2.65744	2.65703	0.000	2.34	1.89	2.24	
28			9/2	2.67312	2.67578	−0.003	2.46	2.04	2.33	
29			7/2	2.68694	2.69193	−0.005	2.61	2.25	2.49	
32	$3d^6(^3F)4s$	$b\ ^4F$	9/2	2.80250	2.80665	−0.004	9.00×10^{-1}	9.26×10^{-1}	8.30×10^{-1}	
33			7/2	2.82671	2.82812	−0.001	1.06	1.08	9.87×10^{-1}	
34			5/2	2.84584	2.84412	0.002	1.33	1.33	1.24	
35			3/2	2.86020	2.85552	0.005	1.72	1.66	1.61	
36	$3d^54s^2$	$a\ ^6S$	5/2	2.89310	2.89102	0.002	2.25×10^{-1}	2.41×10^{-1}	2.33×10^{-1}	0.23(3)[d]
37	$3d^6(^3G)4s$	$a\ ^4G$	11/2	3.15197	3.15277	−0.001	9.34×10^{-1}	9.09×10^{-1}	9.60×10^{-1}	0.75(1)[e]
39			9/2	3.20112	3.19945	0.002	8.76×10^{-1}	8.47×10^{-1}	8.62×10^{-1}	
40			7/2	3.22278	3.22131	0.001	8.60×10^{-1}	7.63×10^{-1}	8.64×10^{-1}	
41			5/2	3.22964	3.23046	−0.001	8.74×10^{-1}	7.58×10^{-1}	8.75×10^{-1}	0.65(2)[e]
38	$3d^6(^3P)4s$	$b\ ^2P$	3/2	3.19432	3.19725	−0.003	1.71	1.87	1.46	
44			1/2	3.34251	3.33923	0.003	1.39	1.52	1.20	
42	$3d^6(^3H)4s$	$b\ ^2H$	11/2	3.24671	3.24469	0.002	4.18	5.75	3.71	3.8 (3)[e]
43			9/2	3.26469	3.26733	−0.003	9.64	1.33×10^1	1.16×10^1	
45	$3d^6(^3F)4s$	$a\ ^2F$	7/2	3.38551	3.38662	−0.001	1.76	1.77	1.52	
46			5/2	3.42483	3.42449	0.000	2.91	2.90	2.53	
47	$3d^6(^3G)4s$	$b\ ^2G$	9/2	3.76784	3.76770	0.000	3.94	3.42	3.49	
48			7/2	3.81417	3.81431	−0.000	4.09	3.52	3.63	
49	$3d^6(^3D)4s$	$b\ ^4D$	1/2	3.88885	3.88870	−0.000	6.32×10^{-1}	5.92×10^{-1}	6.27×10^{-1}	0.54(3)[e]
50			3/2	3.88836	3.88919	−0.000	6.38×10^{-1}	5.99×10^{-1}	6.38×10^{-1}	
51			5/2	3.89333	3.89161	0.002	6.31×10^{-1}	5.92×10^{-1}	6.34×10^{-1}	
52			7/2	3.90676	3.90342	0.003	5.75×10^{-1}	5.46×10^{-1}	5.78×10^{-1}	0.53(3)[d]
53	$3d^7$	$b\ ^2F$	5/2	3.94353	3.94416	−0.001	3.32		2.50	
54			7/2	3.96910	3.96738	0.002	2.63		2.13	
55	$3d^6(^1I)4s$	$a\ ^2I$	13/2	4.07746	4.07606	0.001	2.61		2.38	
56			11/2	4.07887	4.08031	−0.001	3.19		2.91	
57	$3d^6(^1G)4s$	$c\ ^2G$	9/2	4.14972	4.14932	0.000	9.84×10^{-1}		7.30×10^{-1}	

TABLE II. (*Continued*.)

Level				Energy (eV)			Lifetime (s)			
Index	Configuration	Term	J	Present	NIST[a]	Diff.	Present	B2016[b]	HD2011[c]	Expt.
58			7/2	4.15387	4.15363	0.000	1.03		6.58×10^{-1}	
59	$3d^6(^3D)4s$	$b\ ^2D$	3/2	4.46916	4.47910	−0.010	7.71×10^{-1}		6.48×10^{-1}	
60			5/2	4.50381	4.49479	0.009	6.12×10^{-1}		5.13×10^{-1}	
61	$3d^6(^1S)4s$	$a\ ^2S$	1/2	4.61565	4.61559	0.000	5.68×10^{-1}		5.19×10^{-1}	
62	$3d^6(^1D)4s$	$c\ ^2D$	5/2	4.72457	4.73176	−0.007	6.45×10^{-1}		6.59×10^{-1}	
63			3/2	4.74727	4.73799	0.009	5.76×10^{-1}		5.65×10^{-1}	
64	$3d^6(^5D)4p$	$z\ ^6D^o$	9/2	4.76109	4.76831	−0.007	3.17×10^{-9}			$3.68 \times 10^{-9}(7)$[f]
65			7/2	4.79029	4.79324	−0.003	3.19×10^{-9}			$3.67 \times 10^{-9}(9)$
66			5/2	4.81801	4.81790	0.000	3.20×10^{-9}			$3.69 \times 10^{-9}(5)$
67			3/2	4.83953	4.83702	0.003	3.21×10^{-9}			$3.73 \times 10^{-9}(7)$
68			1/2	4.85299	4.84894	0.004	3.21×10^{-9}			$3.68 \times 10^{-9}(11)$
69	$3d^6(^5D)4p$	$z\ ^6F^o$	11/2	5.19807	5.20338	−0.005	2.58×10^{-9}			$3.20 \times 10^{-9}(5)$
70			9/2	5.21950	5.22157	−0.002	2.63×10^{-9}			$3.28 \times 10^{-9}(4)$
71			7/2	5.23748	5.23673	0.001	2.65×10^{-9}			$3.25 \times 10^{-9}(6)$
72			5/2	5.25162	5.24885	0.003	2.66×10^{-9}			$3.30 \times 10^{-9}(5)$
73			3/2	5.26140	5.25709	0.004	2.67×10^{-9}			$3.45 \times 10^{-9}(12)$
74			1/2	5.26713	5.26187	0.005	2.68×10^{-9}			
75	$3d^6(^5D)4p$	$z\ ^6P^o$	7/2	5.29210	5.28895	0.003	2.93×10^{-9}			$3.71 \times 10^{-9}(4)$
76			5/2	5.36066	5.36090	−0.000	2.91×10^{-9}			$3.75 \times 10^{-9}(10)$
77			3/2	5.40511	5.40831	−0.003	2.89×10^{-9}			$3.70 \times 10^{-9}(12)$
78	$3d^6(^5D)4p$	$z\ ^4F^o$	9/2	5.48707	5.48414	0.003	3.29×10^{-9}			$3.72 \times 10^{-9}(10)$
80			7/2	5.55079	5.54877	0.002	3.14×10^{-9}			$3.59 \times 10^{-9}(10)$
85			5/2	5.58996	5.58920	0.001	3.16×10^{-9}			$3.55 \times 10^{-9}(8)$
87			3/2	5.61459	5.61522	−0.001	3.20×10^{-9}			
79	$3d^6(^5D)4p$	$z\ ^4D^o$	7/2	5.50965	5.51071	−0.001	2.74×10^{-9}			$2.97 \times 10^{-9}(4)$
81			5/2	5.55187	5.55261	−0.001	2.76×10^{-9}			$2.90 \times 10^{-9}(6)$
84			3/2	5.58449	5.58477	−0.000	2.74×10^{-9}			$2.91 \times 10^{-9}(9)$
86			1/2	5.60521	5.60489	0.000	2.69×10^{-9}			
88	$3d^6(^5D)4p$	$z\ ^4P^o$	5/2	5.82516	5.82322	0.002	3.20×10^{-9}			$3.27 \times 10^{-9}(6)$
89			3/2	5.87575	5.87559	0.000	3.21×10^{-9}			$3.23 \times 10^{-9}(9)$
90			1/2	5.90427	5.90488	−0.001	3.21×10^{-9}			
100	$3d^5(^6S)4s4p$	$z\ ^8P^o$	5/2	6.48856	6.48435	0.004	7.57×10^{-6}			
101			7/2	6.51981	6.51944	0.000	5.27×10^{-6}			
102			9/2	6.56098	6.56697	−0.006	7.60×10^{-5}			
138	$3d^5(^6S)4s4p$	$y\ ^6P^o$	3/2	7.69120	7.68391	0.007	4.19×10^{-9}			$3.90 \times 10^{-9}(20)$[g]
139			5/2	7.69997	7.69310	0.007	4.05×10^{-9}			$3.80 \times 10^{-9}(20)$
145			7/2	7.70479	7.70830	−0.004	3.79×10^{-9}			$3.65 \times 10^{-9}(20)$

[a]NIST [25].
[b]Bautista *et al.* [19].
[c]Deb and Hibbert [23].
[d]Rostohar *et al.* [33].
[e]Gurell *et al.* [34].
[f]Schnabel *et al.* [35].
[g]Li *et al.* [36].

energy levels is considerably better than in any other previous scattering calculations for Fe II, due to the semiempirical fine-tuning procedure discussed above. Our fine-tuning procedure is designed not just to get close agreement with observed energies; this procedure also includes all strong CI effects and leads to better spin-orbit term mixing.

The radiative data, along with collision strengths, are the important part of the plasma modeling. The Fe II spectrum contains many metastable levels. They decay to lower levels only via forbidden electric quadrupole ($E2$) and magnetic dipole ($M1$) transitions. Table III contains the present results for the line strengths, oscillator strengths, and decay probabilities for both dipole-allowed ($E1$) and dipole-forbidden ($M1$ and $E2$) transitions between all levels included in our scattering calculations. These results can be used to estimate the lifetimes of the excited levels. Comparison of the present lifetimes with available experimental values and the most recent theoretical calculations is given in Table II.

First we discuss the low-lying even-parity metastable states. The comprehensive comparison of the lifetimes for the first 52 levels in Fe II has been recently provided by Bautista *et al.* [19]. Their recommended values are based on the analysis of data

TABLE III. Line strengths, oscillator strengths, and transition probabilities for $E1$, $E2$, and $M1$ transitions in Fe II.

i	k	Type	λ (Å)	S	f_{ik}	A_{ki} (s^{-1})
1	2	$E2$	259883.22	3.30	3.15×10^{-15}	3.89×10^{-10}
1	2	$M1$	259883.22	1.12×10^{1}	1.74×10^{-8}	2.14×10^{-3}
1	3	$E2$	149771.44	9.02×10^{-1}	4.51×10^{-15}	2.23×10^{-9}
1	6	$E2$	53401.69	1.74×10^{-2}	1.92×10^{-15}	4.49×10^{-9}
1	6	$M1$	53401.69	1.34×10^{-3}	1.01×10^{-11}	2.37×10^{-5}
1	7	$E2$	41149.94	4.43×10^{-3}	1.07×10^{-15}	5.26×10^{-9}
1	7	$M1$	41149.94	1.59×10^{-4}	1.57×10^{-12}	7.71×10^{-6}
1	8	$E2$	35236.32	3.40×10^{-4}	1.30×10^{-16}	1.17×10^{-9}
1	10	$E2$	12570.21	7.06×10^{-3}	5.97×10^{-14}	3.15×10^{-6}
1	10	$M1$	12570.21	3.17×10^{-3}	1.02×10^{-10}	5.38×10^{-3}
1	64	$E1$	2600.17	2.39×10^{1}	2.79×10^{-1}	2.75×10^{8}
1	65	$E1$	2586.65	6.84	8.03×10^{-2}	1.00×10^{8}
1	69	$E1$	2382.76	3.11×10^{1}	3.96×10^{-1}	3.88×10^{8}
1	70	$E1$	2374.46	3.17	4.05×10^{-2}	4.80×10^{7}
1	71	$E1$	2367.59	2.60×10^{-2}	3.33×10^{-4}	4.96×10^{5}
1	75	$E1$	2344.21	1.16×10^{1}	1.50×10^{-1}	2.27×10^{8}
1	78	$E1$	2260.78	1.72×10^{-1}	2.31×10^{-3}	3.02×10^{6}
1	79	$E1$	2249.88	1.34×10^{-1}	1.81×10^{-3}	2.98×10^{6}
1	80	$E1$	2234.45	1.40×10^{-3}	1.90×10^{-5}	3.17×10^{4}

obtained from different computational models. The lifetimes of Deb and Hibbert [23] are based on a large-scale CI calculation of the $M1$ and $E1$ transitions among the levels belonging to the $3d^6 4s$, $3d^7$, and $3d^5 4s^2$ configurations. They used very extensive CI expansions, including the $3s$ and $3p$ electron promotions, and they also applied semiempirical corrections to the diagonal elements of the Hamiltonian matrix so that the energy eigenvalues matched experimental energy differences. To estimate the accuracy of lifetimes for the metastable levels, Fig. 2 displays the ratios of lifetimes for the lowest 63 levels in Fe II. As seen from the figure, most of the lifetimes agree, with a few exceptions, within 20%, with average difference being about 12%. The dispersion between lifetimes obtained in different models can serve as an uncertainty indicator; however, further analysis is needed for the individual levels and transitions.

The biggest difference was found for the level $3d^7\ {}^4F_{9/2}$, but there is close agreement for other J levels of this term. This can be explained by the fact that the lifetime for the ${}^4F_{9/2}$ level is mainly determined by a single $M1$ transition, $3d^7\ {}^4F_{9/2}$–$3d^6 4s\ {}^4D_{9/2}$, to the ground state. For the higher ${}^4F_{7/2,5/2,1/2}$ levels, the lifetime is determined by the $M1$ transitions within a multiplet. The dipole $M1$ matrix elements do not involve the radial functions, and $M1$ transition rates within a multiplet depend only on the energy difference and the leading configuration coefficient. For this reason, most calculations provide close results for spectroscopically pure states, where the leading coefficient is close to unity. For transitions between levels from different LS states, the rates are strongly dependent on the mixing between different LS terms, usually on rather small CI coefficients in the wave functions for the two levels. These coefficients strongly depend on the model, and the different methods for such transitions give very different results, which even differ by several orders of magnitude.

For other states presented in Table II, the difference between lifetimes mainly depends on the LS term and configuration mixing, and to a lesser extent on the J value. This indicates the importance of configuration mixing and correct energy difference, whereas the spin-orbit mixing inside the given multiplet is approximately the same. A large difference (around 35%) was also found for the $3d^7\ {}^4P$ and $3d^6({}^3P)4s\ {}^2H$ levels. The lifetimes of the $3d^7\ {}^4P$ levels are mainly determined by the $E2$ transitions to the lower $3d^7\ {}^4F$ states. Because the matrix elements here are defined by the leading configurations with coefficients close to unity, the differences between calculations are most likely due to the different values for the quadrupole radial integrals. The radial integrals, in turn, depend on the $3d$ orbital. In the present calculations we use the configuration-dependent $3d$ orbitals which include the corresponding relaxation effects. The lifetimes of the $3d^6({}^3P)4s\ {}^2H$ levels are also mainly defined by the $E2$ transitions to the $3d^7\ {}^4P$ levels due to large admixture of the ${}^4G$ term. In this case, the spin-orbit interaction plays the decisive role and the differences between calculations are again due to the differing values of the term-mixing coefficients. All calculations agree with available experimental values within 25%, with the dispersion between

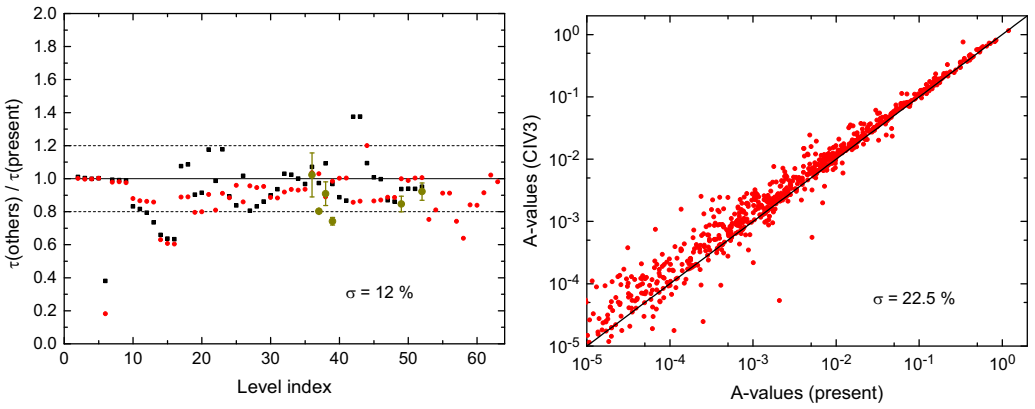

FIG. 2. Left panel: Comparison of lifetimes for the first 63 even-parity metastable levels in Fe II. Red circles, Deb and Hibbert [23]; black squares, Bautista *et al.* [19]; circles with error bars, experimental data [33–36]. Right panel: Comparison of the present radiative rates for the forbidden $E2$ and $M1$ transitions with the CIV3 calculation by Deb and Hibbert [23].

TABLE IV. Comparison of transition probabilities (s^{-1}) for selected $E1$ lines of Fe II. Numbers in parentheses are the experimental uncertainties in percent.

Upper Level	Lower Level	Present	Ref. [35]	Upper Level	Lower Level	Present	Ref. [35]
$z\ ^6D^o_{9/2}$	$a\ ^6D_{9/2}$	2.75×10^8	$2.35 \times 10^8(6)$	$z\ ^4F^o_{5/2}$	$a\ ^4F_{5/2}$	6.53×10^6	$1.13 \times 10^7(13)$
	$a\ ^6D_{7/2}$	4.02×10^7	$3.63 \times 10^7(6)$		$a\ ^4F_{3/2}$	2.12×10^6	$3.27 \times 10^6(24)$
	$a\ ^4D_{7/2}$	2.13×10^5	$3.31 \times 10^5(8)$		$a\ ^4D_{5/2}$	8.60×10^6	$1.06 \times 10^7(24)$
$z\ ^6D^o_{7/2}$	$a\ ^6D_{9/2}$	1.00×10^8	$9.26 \times 10^7(6)$		$a\ ^4D_{3/2}$	2.60×10^8	$2.14 \times 10^8(13)$
	$a\ ^6D_{7/2}$	1.41×10^8	$1.16 \times 10^8(6)$		$a\ ^4P_{5/2}$	2.03×10^5	$1.92 \times 10^5(14)$
	$a\ ^6D_{5/2}$	7.19×10^7	$6.36 \times 10^7(6)$		$a\ ^4P_{3/2}$	9.09×10^5	$9.80 \times 10^5(13)$
	$a\ ^4D_{7/2}$	2.18×10^5	$2.78 \times 10^5(8)$		$b\ ^4F_{5/2}$	2.05×10^5	$2.37 \times 10^5(24)$
$z\ ^6D^o_{5/2}$	$a\ ^6D_{7/2}$	1.63×10^8	$1.43 \times 10^8(6)$		$a\ ^4G_{7/2}$	2.48×10^5	$2.48 \times 10^5(30)$
	$a\ ^6D_{5/2}$	5.36×10^7	$4.84 \times 10^7(8)$	$z\ ^4F^o_{3/2}$	$a\ ^6D_{3/2}$	1.72×10^6	$1.67 \times 10^6(12)$
	$a\ ^6D_{3/2}$	9.51×10^7	$7.92 \times 10^7(6)$		$a\ ^4F_{5/2}$	2.38×10^7	$2.89 \times 10^7(12)$
	$a\ ^4D_{5/2}$	1.92×10^5	$2.31 \times 10^5(8)$		$a\ ^4F_{3/2}$	1.01×10^7	$1.89 \times 10^7(12)$
$z\ ^6D^o_{3/2}$	$a\ ^6D_{5/2}$	2.08×10^8	$1.72 \times 10^8(6)$		$a\ ^4D_{5/2}$	1.08×10^6	$2.78 \times 10^5(12)$
	$a\ ^6D_{3/2}$	3.91×10^6	$4.30 \times 10^6(8)$		$a\ ^4D_{3/2}$	2.74×10^7	$2.89 \times 10^7(12)$
	$a\ ^6D_{1/2}$	9.93×10^7	$9.14 \times 10^7(6)$		$a\ ^4D_{1/2}$	2.46×10^8	$1.89 \times 10^8(12)$
	$a\ ^4D_{3/2}$	1.38×10^5	$2.04 \times 10^5(8)$		$a\ ^4P_{1/2}$	3.52×10^5	$3.00 \times 10^5(12)$
$z\ ^6D^o_{1/2}$	$a\ ^6D_{3/2}$	2.49×10^8	$2.13 \times 10^8(7)$		$b\ ^4F_{3/2}$	1.96×10^5	$1.89 \times 10^5(24)$
	$a\ ^6D_{1/2}$	6.21×10^7	$5.76 \times 10^7(7)$		$a\ ^4G_{5/2}$	3.26×10^5	$5.45 \times 10^5(24)$
$z\ ^6F^o_{11/2}$	$a\ ^6D_{9/2}$	3.88×10^8	$3.13 \times 10^8(2)$	$z\ ^4D^o_{7/2}$	$a\ ^6D_{9/2}$	2.98×10^6	$5.32 \times 10^6(24)$
$z\ ^6F^o_{9/2}$	$a\ ^6D_{9/2}$	4.80×10^7	$4.80 \times 10^7(6)$		$a\ ^4F_{9/2}$	5.52×10^7	$7.09 \times 10^7(6)$
	$a\ ^6D_{7/2}$	3.29×10^8	$2.51 \times 10^8(6)$		$a\ ^4F_{7/2}$	2.03×10^7	$3.04 \times 10^7(6)$
	$a\ ^4D_{7/2}$	3.58×10^6	$5.12 \times 10^6(24)$		$a\ ^4F_{5/2}$	1.87×10^6	$3.17 \times 10^6(24)$
$z\ ^6F^o_{7/2}$	$a\ ^6D_{7/2}$	1.19×10^8	$1.14 \times 10^8(6)$		$a\ ^4D_{7/2}$	2.77×10^8	$2.15 \times 10^8(6)$
	$a\ ^6D_{5/2}$	2.54×10^8	$1.88 \times 10^8(6)$		$a\ ^4P_{5/2}$	5.75×10^6	$8.86 \times 10^6(24)$
	$a\ ^4D_{5/2}$	3.44×10^6	$5.20 \times 10^6(24)$		$b\ ^4P_{5/2}$	4.83×10^5	$7.22 \times 10^5(14)$
$z\ ^6F^o_{5/2}$	$a\ ^6D_{5/2}$	1.67×10^8	$1.40 \times 10^8(6)$		$b\ ^4F_{9/2}$	5.15×10^5	$7.22 \times 10^5(13)$
	$a\ ^6D_{3/2}$	1.94×10^8	$1.50 \times 10^8(6)$	$z\ ^4D^o_{5/2}$	$a\ ^4F_{7/2}$	4.74×10^7	$6.23 \times 10^7(6)$
	$a\ ^4D_{7/2}$	1.08×10^5	$2.70 \times 10^6(8)$		$a\ ^4F_{5/2}$	2.64×10^7	$3.59 \times 10^7(6)$
$z\ ^6F^o_{3/2}$	$a\ ^6D_{5/2}$	3.41×10^7	$3.13 \times 10^7(24)$		$a\ ^4D_{7/2}$	6.74×10^7	$5.70 \times 10^7(6)$
	$a\ ^6D_{3/2}$	2.12×10^8	$1.52 \times 10^8(7)$		$a\ ^4D_{5/2}$	2.08×10^8	$1.69 \times 10^8(6)$
	$a\ ^6D_{1/2}$	1.25×10^8	$1.04 \times 10^8(7)$		$a\ ^4D_{3/2}$	2.95×10^6	$4.75 \times 10^6(8)$
$z\ ^6F^o_{1/2}$	$a\ ^6D_{3/2}$	7.49×10^7	$6.88 \times 10^7(11)$		$a\ ^4P_{5/2}$	1.08×10^6	$1.27 \times 10^6(24)$
	$a\ ^6D_{1/2}$	2.97×10^8	$2.33 \times 10^8(11)$		$a\ ^4P_{3/2}$	4.67×10^6	$6.12 \times 10^6(13)$
$z\ ^6P^o_{7/2}$	$a\ ^6D_{9/2}$	2.27×10^8	$1.70 \times 10^8(11)$		$b\ ^4P_{5/2}$	1.02×10^5	$4.43 \times 10^5(13)$
	$a\ ^6D_{7/2}$	7.79×10^7	$6.03 \times 10^7(11)$		$b\ ^4P_{3/2}$	3.49×10^5	$4.86 \times 10^5(14)$
	$a\ ^6D_{5/2}$	3.21×10^7	$3.21 \times 10^7(11)$		$b\ ^4F_{7/2}$	4.89×10^5	$1.00 \times 10^6(13)$
	$a\ ^4D_{7/2}$	1.73×10^6	$2.21 \times 10^6(23)$	$z\ ^4D^o_{3/2}$	$a\ ^6D_{3/2}$	1.35×10^6	$1.98 \times 10^6(9)$
	$a\ ^6S_{5/2}$	2.28×10^6	$4.22 \times 10^6(23)$		$a\ ^6D_{1/2}$	5.05×10^5	$6.05 \times 10^5(24)$
$z\ ^6P^o_{3/2}$	$a\ ^6D_{5/2}$	8.22×10^7	$5.89 \times 10^7(11)$		$a\ ^4F_{5/2}$	5.03×10^7	$6.49 \times 10^7(7)$
	$a\ ^6D_{3/2}$	1.42×10^8	$1.18 \times 10^8(11)$		$a\ ^4F_{3/2}$	2.80×10^7	$3.85 \times 10^7(24)$
	$a\ ^6D_{1/2}$	1.18×10^8	$8.99 \times 10^7(11)$		$a\ ^4D_{5/2}$	1.14×10^8	$9.35 \times 10^7(7)$
$z\ ^4F^o_{9/2}$	$a\ ^6D_{9/2}$	3.02×10^6	$4.23 \times 10^6(24)$		$a\ ^4D_{3/2}$	1.52×10^8	$1.21 \times 10^8(7)$
	$a\ ^4F_{9/2}$	2.60×10^7	$3.89 \times 10^7(6)$		$a\ ^4D_{1/2}$	1.12×10^7	$1.54 \times 10^7(24)$
	$a\ ^4F_{7/2}$	2.44×10^6	$3.89 \times 10^6(8)$		$a\ ^4P_{3/2}$	2.90×10^6	$3.85 \times 10^6(9)$
	$a\ ^4D_{7/2}$	2.67×10^8	$2.17 \times 10^8(6)$		$a\ ^4P_{1/2}$	3.00×10^6	$3.63 \times 10^6(9)$
	$b\ ^4F_{9/2}$	1.45×10^5	$1.72 \times 10^5(24)$		$b\ ^4P_{3/2}$	2.28×10^5	$2.20 \times 10^5(26)$
$z\ ^4F^o_{7/2}$	$a\ ^6D_{7/2}$	3.71×10^6	$4.41 \times 10^6(13)$		$b\ ^4F_{5/2}$	5.32×10^5	$8.36 \times 10^5(24)$
	$a\ ^6D_{5/2}$	3.54×10^6	$3.87 \times 10^6(13)$	$z\ ^4P^o_{5/2}$	$a\ ^4D_{7/2}$	2.05×10^8	$1.79 \times 10^8(13)$
	$a\ ^4F_{9/2}$	2.83×10^7	$3.44 \times 10^7(13)$		$a\ ^4D_{5/2}$	5.99×10^7	$5.72 \times 10^7(13)$
	$a\ ^4F_{7/2}$	9.02×10^6	$1.51 \times 10^7(13)$		$a\ ^4D_{3/2}$	8.24×10^6	$7.28 \times 10^6(13)$
	$a\ ^4F_{5/2}$	2.33×10^6	$3.87 \times 10^6(13)$		$a\ ^4P_{5/2}$	2.83×10^7	$4.29 \times 10^7(24)$
	$a\ ^4D_{5/2}$	2.69×10^8	$2.15 \times 10^8(13)$		$a\ ^4P_{3/2}$	1.02×10^7	$1.79 \times 10^7(13)$
	$b\ ^4P_{5/2}$	1.50×10^5	$1.72 \times 10^5(24)$		$a\ ^4D_{3/2}$	9.50×10^7	$8.80 \times 10^7(7)$
	$b\ ^4F_{7/2}$	1.98×10^5	$2.26 \times 10^5(24)$		$a\ ^4D_{1/2}$	1.66×10^7	$1.63 \times 10^7(9)$
$z\ ^4F^o_{5/2}$	$a\ ^6D_{5/2}$	3.08×10^6	$3.49 \times 10^6(13)$		$a\ ^4P_{5/2}$	1.90×10^7	$2.01 \times 10^7(9)$
	$a\ ^6D_{3/2}$	2.10×10^6	$2.37 \times 10^6(13)$		$a\ ^4P_{3/2}$	5.87×10^6	$9.43 \times 10^6(9)$
	$a\ ^4F_{7/2}$	2.89×10^7	$3.38 \times 10^7(13)$		$a\ ^4P_{1/2}$	1.55×10^7	$2.39 \times 10^7(9)$

theory and experiment being on the same level as the dispersion of lifetimes obtained in different models.

Comparison of the radiative rates for transitions between individual levels provides more detailed information about agreement between existing data sets. Comparison with the recent CIV3 calculation [23] is given in Fig. 2 for all forbidden $E2$ and $M1$ transitions between the first 63 metastable levels in Fe II. Overall good agreement was found for the stronger lines with A values greater than 10^{-2} s^{-1}, where radiative rates are estimated to be accurate within 20%–30%, or better. As seen from the figure, the weaker transition rates are much less reliable. Both our and CIV3 calculations use the experimental energies, not only for transition energies, but also to enhance the accuracy of the CI mixing coefficients in the wave functions through the fine-tuning procedure. However, dispersion between individual radiative rates increases considerably as their absolute values decrease, to several orders of magnitude. The weak transitions are usually driven by coupling with other configurations or small term admixing. In order to obtain the accurate radiative rate for such transitions one needs to check the convergence in each individual case.

Lifetimes of the higher levels with index 63 and more are defined by strong electric-dipole $E1$ transitions. Comparison with the experimental data in Table II shows that the present calculations reproduce these lifetimes within 10%–25%. The same accuracy may be expected for the strong $E1$ radiative rates. There are a huge number of different experimental measurements and theoretical calculations for the individual $E1$ transitions. Most of them are presented in the NIST critical compilation. Overall comparison with the existing data is out of scope of the present work. Our main goal here is the calculation of scattering parameters. Note that cross sections for the dipole-allowed transitions at high electron energies are directly proportional to the oscillator strengths, whereas the main contribution to the rate coefficient for the weak spin-forbidden transitions comes from the resonance excitation. In order to illustrate the accuracy of our A values for the individual $E1$ transitions, Table IV compares our radiative rates with the selected experimental data taken from the most recent measurements [35]. These measurements report absolute transition probabilities of 140 Fe II lines in the wavelength range 220–780 nm, with overall uncertainties estimated to be 6% for the strong and up to 26% for the weak transitions. This large set of experimental data can be used for a reliability check of theoretical data. As seen from the table, there is a good agreement in the limits of 25% between experiment and theory for the strong spin-allowed transitions with A values greater than 10^7 s^{-1}. Agreement with weaker lines is more scattered. Weak lines are usually related to the spin-forbidden or two-electron transitions, and depend strongly on the configuration and term mixing. The term mixing in our calculations is handled with our fine-tuning process. As seen from the table, in most cases it results in an accuracy of 20%–50% for transitions with A values greater than 10^5 s^{-1}. For weaker transitions the disagreement may reach several orders of magnitude. We omit such transitions from comparison because this comparison will not provide any useful information.

The above comparison of radiative rates and lifetimes with experimental values is given primarily to illustrate the accuracy of the present target wave functions. We illustrated that our target states accurately reproduce the strong $E1$ as well as $M1$ and $E2$ transitions in Fe II. Note that our target expansions are restricted in size to keep further scattering calculations manageable. Further improvement of the accuracy of radiative data, especially for the weaker lines, requires the further extension of the configuration expansions. Such calculations devoted to the detailed analysis of the individual radiative lines will be presented in a separate paper.

B. Collision strengths and thermally averaged collision strengths

We begin our discussion with collision strengths for the fine-structure forbidden transitions between the low-lying levels of Fe II. Figure 3 shows collision strengths for excitation of the $3d^64s\ ^6D_{7/2}$ and $3d^7\ ^4D_{9/2}$ levels from the ground $3d^64s\ ^6D_{9/2}$ level. The same transitions were also discussed by Ramsbottom *et al.* [17]. We concentrate on the low-energy resonance region up to 0.5 Ry, where collision strength exhibits rich resonance structures. The resonance structures considerably exceed the background collision strength and provide dominant contribution to the rate coefficients at lower temperatures. It is a typical behavior for the forbidden transitions found in many other electron-ion scattering processes.

The resonance structure exhibits a set of Rydberg series of resonances converging to the different target thresholds. For the $3d^64s\ ^6D_{9/2}$–$3d^64s\ ^6D_{7/2}$ (1-2) transition, the most noticeable Rydberg series are lying below the $3d^64s\ ^4D_{7/2}$, $3d^64p\ ^4D_{9/2}$, and $3d^64p\ ^6F_{11/2}$ thresholds. Most likely, these series of the narrow resonances are related to the $3d^64snl$ or $3d^64pnl$ states, created by trapping of the scattering electron to the highly excited nl states with simultaneous $4s$-$4p$ excitation of the valence $4s$ electron (or just changing the coupling scheme). Note that above the $3d^64p\ ^6F$ threshold the resonance structures diminish considerably and do not contribute much to the excitation process. There is also a set of strong and wide resonances, especially in the region from 0.2 to 0.3 Ry. The large width of these resonances indicates strong interaction between the $3d$ electrons. We suggest that these resonances have the principal configuration $3d^74p$ or $3d^8$. Comparisons are made with most recent and extensive R-matrix calculations available in the literature. We will use the following abbreviations for different calculations: RM-142 for the 142 target-state R-matrix calculations of Zhang and Pradhan [9]; RM-262 for the 262 target-state R-matrix calculations of Ramsbottom *et al.* [17]; RM-AV for the effective collision strengths obtained by Bautista *et al.* [19] as an average from different R-matrix calculations. The present calculations will be denoted as BSR-340. The resonance structure for this transition is very close in form to the resonance structure found in the RM-262 calculations of Ramsbottom *et al.* [17], but differs in many details from the resonance structure found in the RM-142 calculations of Zhang and Pradhan [9]. The RM-142 resonance structure is not as strong, partly because Zhang and Pradhan's CC expansion does not include the $3d^7$ double excitation terms lying in this energy region.

The Maxwellian averaged effective collision strength for the $3d^64s\ ^6D_{9/2}$–$3d^64s\ ^6D_{7/2}$ transition is presented in Fig. 3, lower panels. As seen from the Fig. 3, the rate coefficients obtained in

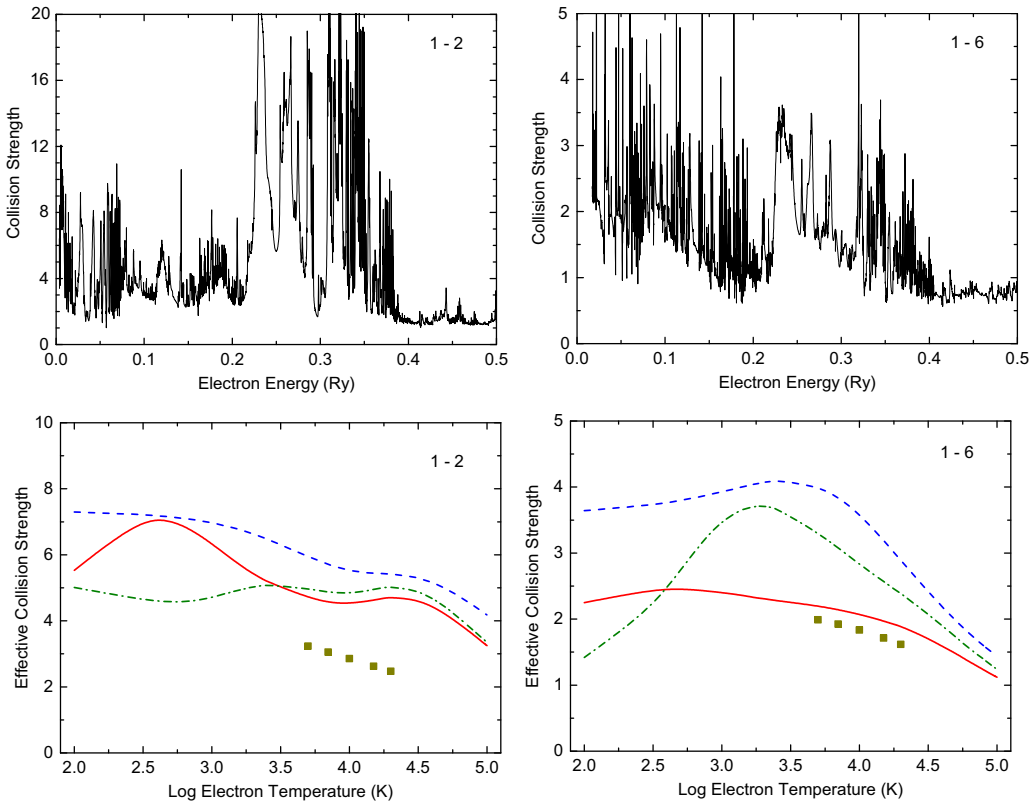

FIG. 3. Upper panel: Collision strengths for the $3d^6 4s\ ^6D_{9/2}$–$3d^6 4s\ ^6D_{7/2}$ (1-2) and $3d^6 4s\ ^6D_{9/2}$–$3d^7\ ^4D_{9/2}$ (1-6) fine-structure transitions. Lower panel: Effective collision strength for the (1-2) and (1-6) transitions. Solid curve, present BSR-340 model; dash-dotted curve, the RM-262 calculations of Ramsbottom *et al.* [17]; dashed curve, the RM-142 calculations of Zhang and Pradhan [9]; solid rectangles, the RM-AV calculations of Bautista *et al.* [19].

different models are rather different both in magnitude and in the temperature behavior. The closest agreement is obtained with the RM-262 calculations of Ramsbottom *et al.* [17], however, only for higher temperatures. For low temperature around 500 K, our rates show the maximum which is absent in the RM-262 calculations. As seen from the figure, this low-temperature maximum is due to the resonances lying close to excitation thresholds. This set of strong resonances is shifted to the higher energies in the RM-262 calculations due to the higher excitation thresholds in the RM-262 model. Strong dependence of the resonance structure and its contribution to the rate coefficients on the position of excitation thresholds was also clearly illustrated by Bautista *et al.* [19]. By comparing the results from various models Bautista *et al.* [19] found that the collision strengths for transitions among levels of the $3d^6 4s\ ^6D$ ground multiplet are greatly enhanced when the excitation threshold are shifted to experimental values. Our target thresholds are very close to the experimental values, so we may expect the most accurate representation of the resonance structure in our scattering calculations. The RM-142 rate coefficients of Zhang and Pradhan [9] considerably exceed the present results for all temperatures, whereas the recommended rate coefficients of Bautista *et al.* [19] are considerably lower than all other rates. This indicates that these calculations predict different values of both the resonance contributions and the background collision strengths. The same trends were found to occur for all other fine-structure transitions among the ground-state levels.

Transition $3d^6 4s\ ^6D_{9/2}$–$3d^7\ ^4D_{9/2}$ (1-6) in Fig. 3 represents the transition between different terms. We again see a rich resonance structure which, however, is less intense in magnitude than for the (1-2) transition considered above. Our resonance structure qualitatively agrees with the resonance structure from the RM-262 calculations; however, there is noticeable difference in the positions and widths of strong resonances in the region from 0.2 to 0.3 Ry. The different calculations again predict rather different rate coefficients. For this transition our effective collision strengths are closest to the RM-AV results of Bautista *et al.* The RM-262 rates show a maximum at intermediate temperatures which is not predicted in our calculations. The RM-142 rate coefficients considerably exceed other results, especially at low temperatures. It may be pointed out that the recoupling transformation method employed in these calculations does not appear to reproduce the resonance structure accurately enough. We suggest that the contribution of some high-lying resonances in the RM-262 model is highly overestimated. Rate coefficients from different calculations converge to each other at high temperatures, indicating the similar background collision strengths in the different models.

Above examples show that there are considerable discrepancies between the existing calculations for the rate coefficients of forbidden transitions in Fe II. A global comparison between the present BSR-346 results and the effective collision strengths obtained previously is presented in Fig. 4 at three different temperatures. In this figure we consider only the

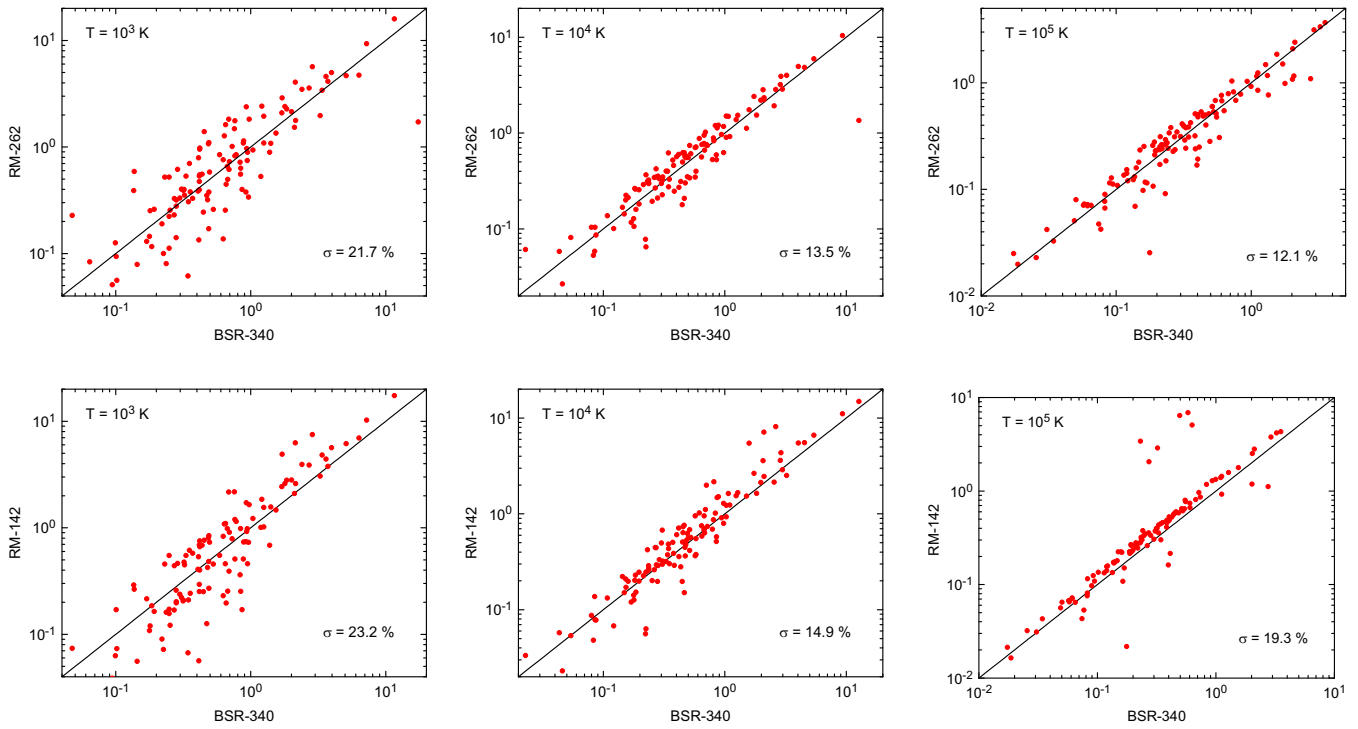

FIG. 4. Comparison of effective collision strengths obtained in the present BSR-340 model with the RM-262 [17] (upper panels) and RM-142 [9] (lower panels) for three temperatures. Also indicated in the panels is the average deviation σ from the BSR-340 results. Comparison includes the forbidden transitions between the first 52 even-parity levels of Fe II.

forbidden transitions among low-lying even-parity states. As seen from the figure, the worst agreement between calculations is observed at low temperatures, with average deviations of around 22%; however, for the individual transitions some rates exhibit substantial disagreement. At low temperatures, the effective collision strength crucially depends on the near-threshold resonance structure. This resonance structure depends in turn on the target excitation energies and the size of CC expansions. We use the experimental excitation thresholds and employed the most extensive CC expansion, which allows us to argue that the present resonance structure is most accurate. The energy mesh used in the RM-142 calculation is much coarser than in the other calculations. This also may lead to a poor account of the resonance contributions. Note also that the resonance structure for the forbidden transitions extends mainly up to ~0.4 Ry, the region where the channels of odd-parity states $3d^6 4p$ begin to open. For higher electron energies the resonance contribution greatly diminishes.

As seen from the Fig. 4, agreement considerably improves for the intermediate temperatures around $T = 10^4$ K. The average deviation for these temperatures decreases to 15%. Except for a few transitions, the agreement further improves for the higher temperatures, indicating that all calculations generally agree on background cross sections, and the differences are mostly due to the resonance structures. However, there are transitions where the disagreement increases with temperature, though the influence of the resonance structure is minimal. There may be several reasons for this. It may be caused by partial wave convergence, different target-state expansions and thereby different background collision strengths, or the appearance of pseudoresonance structures at higher electron energies. There are many examples of the strong pseudoresonance structures that can substantially change the cross sections (see, e.g., [38]). This reason appears the most probable as to why the RM-142 calculation shows very different rates for some transitions, whereas the majority of the rates are in very close agreement with the present calculations at $T = 10^5$ K. Overall, the comparison in Fig. 4 can serve as an accuracy estimation for the existing data sets.

The forbidden transitions between the 52 lowest levels were recently investigated carefully by Bautista *et al.* [19]. They used two different methods, specifically *R*-matrix+ICFT and the fully relativistic DARC approach [39]. They also investigated the sensitivity of collision strengths to the details of the scattering calculations, such as size of the target and close-coupling expansions, shifting the excitation thresholds to the experimental positions, or size of the *R*-matrix box. The comparison of effective collision strengths from different models was presented at 10^4 K, the temperature where Fe II is most frequently found. The statistical dispersion of results from different models is assumed as an accuracy indicator. In particular, they estimated uncertainties in the range of 10%-20% for excitations from the lower nine levels. However, if the complete collision inventory is considered, the effective collision strength discrepancies vary widely, reaching factors of two or more in some cases. Figure 5 compares our effective collision strengths with the recommended data of Bautista *et al.* obtained as the average of results from their numerous models (denoted as RM-AV). We see large discrepancies between these two sets, which are much larger than the differences with the RM-142 and the RM-262 effective

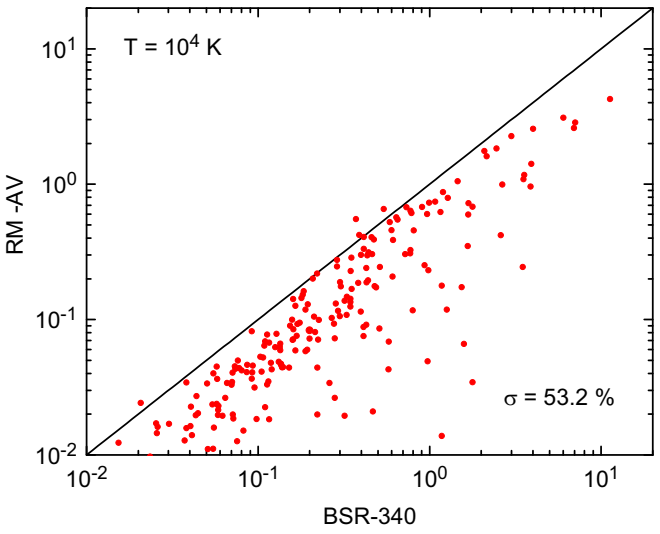

FIG. 5. Comparison of effective collision strengths obtained in the present BSR-340 model with the RM-AV results of Bautista *et al.* [19] at temperature of 10^4 K.

collision strengths discussed above. Overall, the RM-AV effective collision strengths are systematically lower than the present results, with the average relative deviation of more than 50%. Note that for the subset of data presented in their paper as a comparison of different models, much better agreement is found with the DARC results than with the R-matrix+ICFT calculations. We may conclude that the averaging of the "chaotic" data sets does not lead to better accuracy. Instead, the accuracy estimations based on the careful analysis of the convergence of target and close-coupling expansions are more preferable.

Now we turn to the discussion of the electric-dipole transitions which involve the $3d^6 4p$ and $3d^5 4s 4p$ odd-parity levels of Fe II. Examples of collision strengths and thermally averaged collision strengths for electron-impact excitation to the lowest odd-parity states are given in Fig. 6. We choose excitation of the $3d^6 4p\ {}^6D^o_{9/2}$ and $3d^6 4p\ {}^6F^o_{11/2}$ levels from the ground $3d^6 4s\ {}^6D_{9/2}$ level as these were also discussed by Zhang and Pradhan [9] and Ramsbottom *et al.* [18]. Both of these transitions are the strong electric-dipole transitions, which exhibit the characteristic $\ln(E)$ behavior at almost all energies. The resonance structure at low energies is very scarce and provides only a limited contribution to the rate coefficients. For the $3d^6 4s\ {}^6D_{9/2}$–$3d^6 4p\ {}^6D^o_{9/2}$ (1-64) transition, our collision strengths agree closely with the RM-142 calculations by Zhang and Pradhan, and are systematically lower by 20%–30% than the RM-262 results of Ramsbottom *et al.* This difference can be caused by several reasons. First, we should be sure that all partial wave contributions were correctly incorporated. Due to the long-range nature of the Coulomb potential, the dominant contribution to the dipole-allowed transitions comes from the partial waves with large total orbital momentum, especially for higher electron energies. Ramsbottom *et al.* [18] devoted a large part of their discussion to this problem and concluded that in order to obtain convergence of the electron-impact excitation collision strengths for the allowed transitions in Fe II, it is necessary to include contributions from partial waves up to about $L = 50$ explicitly, with additional accounting for contributions from even higher partial waves via a top-up procedure. They also suggested that the incomplete partial wave contribution in the RM-142 calculations of Zhang and Pradhan was the primary reason for disagreement between these two calculations. We argue that the partial wave convergence can be reached for much lower L. Our collision strengths obtained with direct calculations up to $L = 50$, followed by the top-up procedure, differ only in limits of 1%–2% from the test results with direct calculations up to $L = 25$ and followed by the top-up procedure. Besides, all discussed collision strengths behave asymptotically as $\ln(E)$. This fact also indicates that top-up correction was correctly implied in all calculations.

The differences with the RM-262 collision strengths are most likely due to the different representation of target states, and as a consequence, differences in oscillator strengths for the electric-dipole transitions. For higher energies, collision strengths for dipole-allowed transitions are proportional to the oscillator strengths, so their accuracy is very important for accurate description of the scattering process at higher energies. Our oscillator strength for the $3d^6 4s\ {}^6D_{9/2}$–$3d^6 4p\ {}^6D^o_{9/2}$ transition is 0.279, which is 12% lower than the f-value of 0.311 from the RM-262 calculations. This partly explains why our collision strengths are systematically lower than the RM-262 results. Note that our oscillator strength is even larger than the experimental oscillator strength of 0.238 derived from the radiative rates of Schnabel *et al.* [35] presented in Table IV. We then may suppose that actual collision strengths should be even lower than presented in Fig. 6. The corresponding Maxwellian averaged effective collision strengths for this transition, plotted in the lower panel in Fig. 6, show agreement and disagreement similar to those for the corresponding collision strengths. Our effective collision strengths are systematically lower than the RM-262 values, and agree closely with the RM-142 data at higher temperatures. The RM-142 data exceed our effective collision strengths at temperatures below 5000 K, which may indicate the larger contribution of the resonances in their calculations. Note that we compare the RM-142 effective collision strengths based on the CHIANTI database [10], which provides a more extended set of data than provided in the original publication [9].

A similar picture is observed for the $3d^6 4s\ {}^6D_{9/2}$–$3d^6 4p\ {}^6F^o_{11/2}$ transition, presented in the left panel of Fig. 6. Again the RM-262 collision strengths exceed the present results, whereas our collision strengths agree closely with the RM-142 data for all electron energies. The curves have similar shape but different slope which is defined by the oscillator strength. Our oscillator strength for this transition, 0.396, is lower by 12% than the f value of 0.446 from the RM-262 calculations, but exceeds the experimental value of 0.319 [35]. The corresponding Maxwellian averaged effective collision strengths from RM-262 and the present calculations differ in the same proportion as the collision strengths. The RM-142 calculation agrees with the present results only for higher temperatures, whereas it exceeds both the present and RM-262 effective collision strengths at lower temperature below 10^4 K. It can be explained by overestimated resonance contributions in the LS plus frame transformation method employed in the RM-142 calculations.

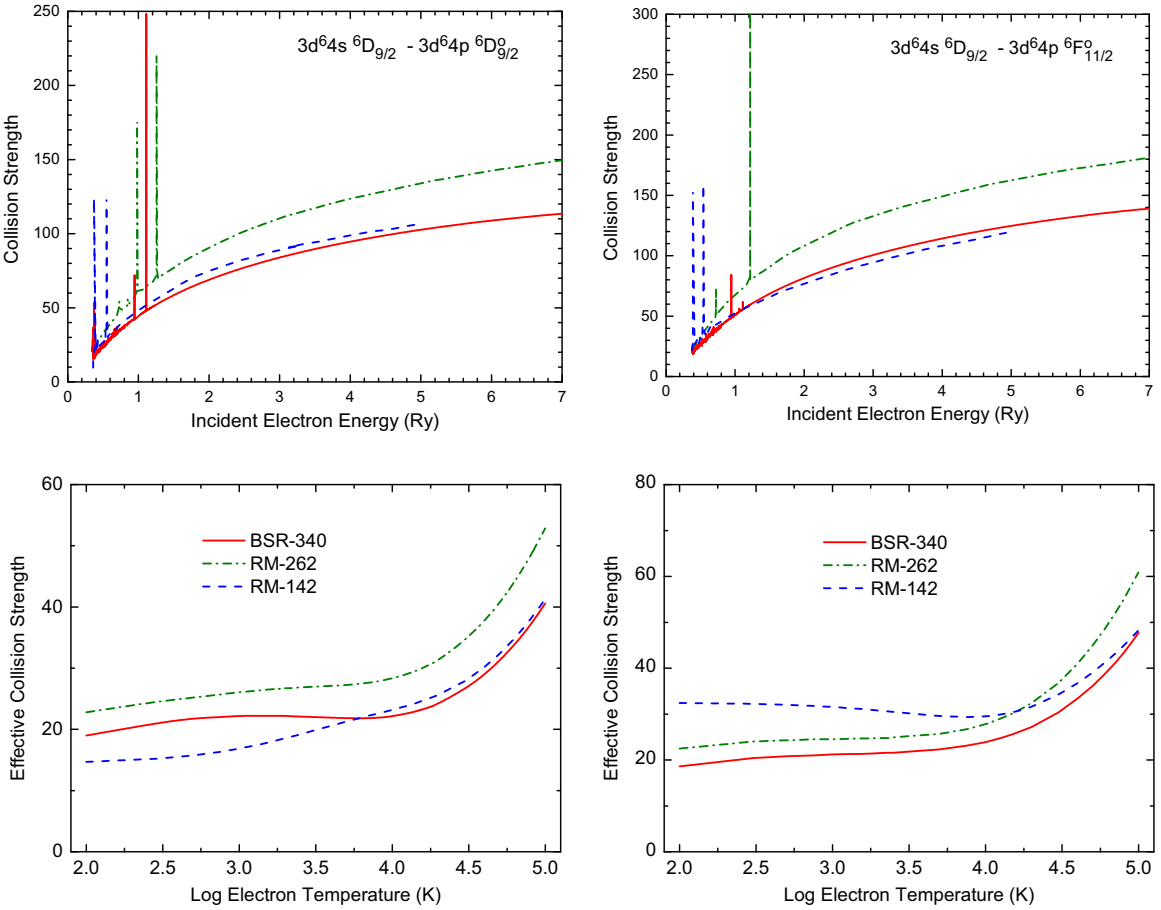

FIG. 6. Upper panels: Collision strengths for the $3d^6 4s\,^6D_{9/2}$–$3d^6 4p\,^6D^o_{9/2}$ (1-64) and $3d^6 4s\ ^6D_{9/2}$–$3d^6 4p\ ^6F^o_{11/2}$ (1-69) fine-structure transitions. Lower panels: Effective collision strength for the (1-64) and (1-69) transitions. Solid curve, present BSR-340 model; dot-dashed curve, the RM-262 calculations of Ramsbottom *et al.* [17]; dashed curve, the RM-142 calculations of Zhang and Pradhan [9].

The overall comparison of the effective collision strengths for the electric-dipole-allowed transitions is given in Fig. 7 for temperature $T = 10^4$ K. Dispersion between the present and RM-262 results is considerable, with the average relative deviation around 42%. The general tendency is that the RM-262 effective collision strengths exceed the present values for the most of the transitions. If we consider only the transitions from the levels of the ground configuration (presented in the

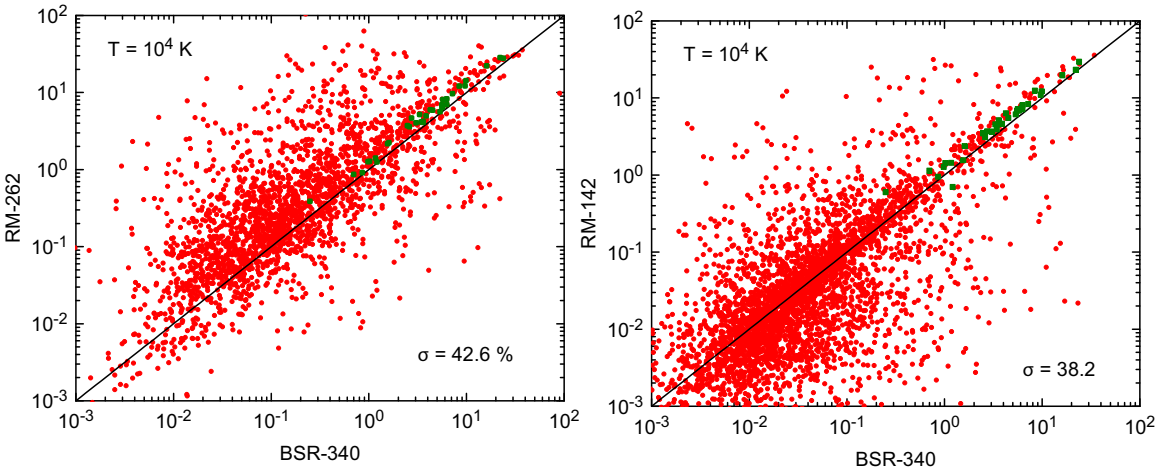

FIG. 7. Comparison of effective collision strengths obtained in the present BSR-340 model with RM-262 [17] (left panel) and RM-142 [9] (right panel) for electron temperature $T = 10^4$ K. Also indicated in the panels is the average deviation σ from the BSR-340 results. The squares in the left panel represent transitions from the ground level only.

figure with squares), the agreement is much better, with the average relative deviation of around 10%. The large differences appear for transitions between excited states, beginning for transitions from the first excited $3d^7\,{}^4F$ term. Some differences reach several orders of magnitude, both for weak and strong transitions. Such large differences may be due to the different target representations in the two calculations. The restricted target expansions used in the RM-142 calculation leads to inaccurate oscillator strengths and consequently to inaccurate collision strengths. The average deviation of our results from the RM-142 calculation is approximately on the same level as from the RM-262 results; however, the deviation here is more chaotic, with no systematic trend. Note that comparison with the RM-142 calculation in Fig. 7 additionally includes the nondipole transitions which are not presented in the RM-262 results.

The entire tables of energies, radiative rates, and effective collision strengths for all temperatures and transitions included in the present BSR-340 model can be found in the Supplemental Material [37].

IV. SUMMARY

We have presented effective collision strengths and radiative parameters for all transitions among the 340 fine-structure levels of Fe II, belonging to the lowest $3d^64s$, $3d^54s^2$, $3d^7$, $3d^64p$, and $3d^54s4p$ configurations. The present results considerably expand the existing data sets for Fe II, allowing a more detailed treatment of the available measured spectra from different astrophysical sources. The calculations were performed with the advanced BSR code [20] which employs the *R*-matrix method in the *B*-spline basis. The BSR codes are considerably modified and extended in order to deal with this extremely complicated atomic system. To represent the target states, we use extensive multiconfiguration expansions with carefully chosen configurations. We also employ the term-dependent one-electron orbitals for correct representation of the relaxation effects. To further improve the accuracy of our final collision rates, experimental energies through the fine-tuning process have been used, not only for target level energies, but also to enhance the accuracy of the term-mixing coefficients in the wave functions. This is a distinctive feature of the present calculations that allows us to generate a more accurate description of the Fe II target states than those employed before.

Comparison is made between our work and results available in existing databases. This comparison shows that previous calculations of collision strengths for many transitions are much more uncertain than previously thought. We offer arguments in favor of our results being the most accurate, where differences occur. This is based on the more accurate representation of target states and more extensive close-coupling expansions. It is difficult to place uncertainty bounds on our collision rates. Transitions from the ground multiplet levels are probably correct to within about 10%. For transitions between excited states better accuracy is expected for levels within the well-defined main configurations. Such transitions should be reliable to within 20%–30% or better. For transitions between levels with strong configuration and term mixing, the accuracy of collision strengths is dependent on the accuracy of the mixing. Our fine-tuning process is designed to represent that mixing as accurately as possible. This allows us to assume that an accuracy of about 20%–50% can be achieved in these cases too. This conclusion is supported by the comparison of our radiative rates with available experimental data. If additional factors specific for scattering calculations (such as careful consideration of the resonance structure and partial wave convergence) are treated properly, the accuracy of collision rates should be comparable with the accuracy of radiative rates. Thus, the agreement of our radiative rates with experimental values can also serve as an accuracy estimation for the collision rates. For many transitions this agreement is within 20%–50%; however, for some weak transitions the disagreement can reach to orders of magnitude. These transitions are related to the case where there are considerable cancellation effects due to CI or term mixing, and in this case small changes in mixing can lead to substantial changes in the final collision rates. Such transitions if needed should be considered in the specifically designed calculations, which are concentrated in the individual transitions.

ACKNOWLEDGMENTS

This work was supported by the United States National Science Foundation under Grants No. AST-1714159 and No. PHY-1520970. The numerical calculations were performed on STAMPEDE supercomputer at the Texas Advanced Computing Center and used the Extreme Science and Engineering Discovery Environment (XSEDE), which is supported by National Science Foundation under Grants No. PHY-090031 and No. PHY-170047.

[1] D. M. Meyer, K. M. Lanzetta, and A. M. Wolfe, Astrophys. J. Lett. **451**, L13 (1995).
[2] J. C. Howk and K. R. Sembach, Astrophys. J. Lett. **523**, L141 (1999).
[3] M. A. Dopita, I. R. Seitenzahl, R. S. Sutherland, F. P. A. Vogt, P. F. Winkler, and W. P. Blair, Astrophys. J. **826**, 150 (2016).
[4] B. C. Koo, J. C. Raymond, and H. J. Kim, J. Korean Astron. Soc. **49**, 109 (2016).
[5] P. S. Barklem, Astron. Astrophys. Rev. **24**, 9 (2016).
[6] K. L. Baluja, A. Hibbert, and M. Mohan, J. Phys. B **19**, 3613 (1986).
[7] K. A. Berrington, P. G. Burke, A. Hibbert, M. Mohan, and K. L. Baluja, J. Phys. B **21**, 339 (1988).
[8] A. K. Pradhan and K. A. Berrington, J. Phys. B **26**, 157 (1993).
[9] H. Zhang and A. K. Pradhan, Astron. Astrophys. **293**, 953 (1995).
[10] See http://chiantidatabase.org.
[11] M. A. Bautista and A. K. Pradhan, Astron. Astrophys., Suppl. Ser. **115**, 551 (1996).

[12] M. A. Bautista and A. K. Pradhan, Astrophys. J. **492**, 650 (1998).
[13] P. G. Burke, C. J. Noble, A. G. Sunderland, and V. M. Burke, Phys. Scr. T **100**, 55 (2002).
[14] C. A. Ramsbottom, M. P. Scott, K. L. Bell, F. P. Keenan, B. M. McLaughlin, A. G. Sunderland, V. M. Burke, C. J. Noble, and P. G. Burke, J. Phys. B **35**, 3451 (2002).
[15] C. A. Ramsbottom, C. J. Noble, V. M. Burke, M. P. Scott, and P. G. Burke, J. Phys. B **37**, 3609 (2004).
[16] C. A. Ramsbottom, C. J. Noble, V. M. Burke, M. P. Scott, R. Kisielius, and P. G. Burke, J. Phys. B **38**, 2999 (2005).
[17] C. A. Ramsbottom, C. E. Hudson, P. H. Norrington, and M. P. Scott, Astron. Astrophys. **475**, 765 (2007).
[18] C. A. Ramsbottom, At. Data Nucl. Data Tables **95**, 910 (2009).
[19] M. A. Bautista, V. Fivet, C. Ballance, P. Quinet, G. Ferland, C. Mendoza, and T. R. Kallman, Astrophys. J. **808**, 174 (2015).
[20] O. Zatsarinny, Comput. Phys. Commun. **174**, 273 (2006).
[21] O. Zatsarinny and K. Bartschat, Phys. Rev. A **72**, 020702 (2005).
[22] A. Hibbert, Phys. Scr. T **65**, 104 (1996).
[23] N. C. Deb and A. Hibbert, Astron. Astrophys. **536**, A74 (2011).
[24] C. Froese Fischer, G. Tachiev, G. Gaigalas, and M. R. Godefroid, Comput. Phys. Commun. **176**, 559 (2007).
[25] A. Kramida, Yu. Ralchenko, J. Reader, and NIST ASD Team, NIST Atomic Spectra Database (Ver. 5.3), National Institute of Standards and Technology, Gaithersburg, MD, available at http://physics.nist.gov/asd.
[26] O. Zatsarinny and C. Froese Fischer, Comput. Phys. Commun. **124**, 247 (2000).
[27] O. Zatsarinny and C. Froese Fischer, Comput. Phys. Commun. **180**, 2041 (2009).
[28] P. G. Burke, *R-Matrix Theory of Atomic Collisions* (Springer-Verlag, Berlin, 2011).
[29] S. S. Tayal and O. Zatsarinny, Astrophys. J. **788**, 24 (2014).
[30] S. S. Tayal and O. Zatsarinny, Astrophys. J. **743**, 206 (2011).
[31] S. S. Tayal and O. Zatsarinny, Astrophys. J. **812**, 174 (2015).
[32] See http://www.apap-network.org/codes.
[33] D. Rostohar, A. Derkatch, H. Hartman, S. Johansson, H. Lundberg, S. Mannervik, L. O. Norlin, P. Royen, and A. Schmitt, Phys. Rev. Lett. **86**, 1466 (2001).
[34] J. Gurell, H. Hartman, R. Blackwell-Whitehead, H. Nilsson, E. Bäckström, L. O. Norlin, P. Royen, and S. Mannervik, Astron. Astrophys. **508**, 525 (2009).
[35] R. Schnabel, M. Schultz-Johanning, and M. Kock, Astron. Astrophys. **414**, 1169 (2004).
[36] Z. S. Li, H. Lundberg, U. Berzinsh, S. Johansson, and S. Svanberg, J. Phys. B **33**, 5593 (2000).
[37] See Supplemental Material at http://link.aps.org/supplemental/10.1103/PhysRevA.98.012706 for extensive tables of energies, radiative parameters, and effective collision strengths.
[38] K. Wang, L. Fernandez-Menchero, O. Zatsarinny, and K. Bartschat, Phys. Rev. A **95**, 042709 (2017).
[39] See http://amdpp.phys.strath.ac.uk/rmatrix/ser/darc.